The 27-28 October 1986 FIRE IFO Cirrus Case Study: Comparison of Radiative Transfer Theory with Observations by Satellite and Aircraft

Bruce A. Wielicki and J. T. Suttles
Atmospheric Sciences Division, NASA Langley Research Center
Hampton, Virginia

Andrew J. Heymsfield
National Center for Atmospheric Research, Boulder, Colorado

Ronald M. Welch
South Dakota School of Mines and Technology, Rapid City, South Dakota

James D. Spinhirne and Man-Li C. Wu
NASA Goddard Space Flight Center, Greenbelt, Maryland

David O'C. Starr
NASA Goddard Space Flight Center, Greenbelt, Maryland

Lindsay Parker and Robert F. Arduini
PRC Corporation, Hampton, Virginia

Submitted to
Monthly Weather Review
March 1989

ABSTRACT

Observations of cirrus and altocumulus clouds during the First International Satellite Cloud Climatology Project Regional Experiment (FIRE) are compared to theoretical models of cloud radiative properties. Three tests are performed. First, Landsat radiances are used to compare the relationship between nadir reflectance at 0.83μm and beam emittance at 11.5μm with that predicted for model calculations using spherical and non-spherical phase functions. Good agreement is found between observations and theory when water droplets dominate. Poor agreement is found when ice particles dominate, especially using scattering phase functions for spherical particles. Even when compared to a laboratory measured ice particle phase function (Volkovitskiy et al., 1980), the observations show increased side scattered radiation relative to the theoretical calculations. Second, the anisotropy of conservatively scattered radiation is examined using simultaneous multiple-angle views of the cirrus from Landsat and ER-2 aircraft radiometers. Observed anisotropy gives good agreement with theoretical calculations using the laboratory measured ice particle phase function and poor agreement with a spherical particle phase function. Third, Landsat radiances at 0.83μm, 1.65μm, and 2.21μm are used to infer particle phase and particle size. For water droplets, good agreement is found with King Air FSSP particle probe measurements in the cloud. For ice particles, the Landsat radiance observations predict an effective radius of 60μm versus aircraft observations of about 200μm. It is suggested that this discrepancy may be explained by uncertainty in the imaginary index of ice and by inadequate measurements of small ice particles by microphysical probes.

1. Introduction

Cirrus clouds are perhaps the least understood of the Earth's cloud types. The wide range of sizes and shapes of cirrus particles (Heymsfield and Platt, 1984) greatly complicates efforts to model their radiative properties. Satellite radiometers have difficulty accurately measuring cirrus because of their small optical depths and large spatial variability (Reynolds and Vonder Haar, 1977; Rossow et al, 1985). Even research aircraft find it difficult to sample at cirrus altitudes. Many of the cloud particles are too small to be measured reliably with current instrumentation (Heymsfield and Platt, 1984). In addition, vertical motions are often too weak or transient to be measured.

These difficulties adversely impact several areas of climate research. The International Satellite Cloud Climatology Project (ISCCP) requires a relationship between cirrus visible reflectance and infrared emittance in order to accurately determine cirrus altitudes (Rossow et al, 1985). Yet the accuracy of this relationship is currently unknown. The Earth Radiation Budget Experiment (ERBE) requires models of the anisotropic reflectance of clouds in order to estimate outgoing radiative flux using measurements of outgoing radiance at a single direction (Suttles et al, 1988). Anisotropic models, however, are currently unavailable for cirrus clouds. Finally, attempts to derive cloud particle size using satellite or aircraft radiance measurements near 1.6 and 2.1μm have given highly variable results. Twomey and Cocks (1982) and Rozenberg et al (1974) found anomalously high absorption (i.e., low reflectance) at these wavelengths for optically thick liquid water clouds. Curran and Wu (1982) using SKYLAB measurements found anomalously low absorption (i.e., high reflectance) for optically thick

cirrus. More recently, Foot (1988) found mixed results comparing aircraft microphysics with radiance observations of liquid water clouds and reasonable agreement for an ice cloud case.

The present work continues the effort to both measure and model the radiative properties of cirrus clouds. Aircraft microphysics, aircraft radiometry, aircraft lidar, and satellite radiance measurements are utilized to examine cirrus radiative properties during a Landsat overflight of Lake Michigan on October 28, 1986. The breadth of measurements available for this case allows an examination of all three of the areas of concern mentioned above for a single cirrus cloud field.

Section 2 of the paper discusses the data sources used in the investigation, as well as the navigation and calibration of the various radiometric measurements. Section 3 outlines the radiative transfer model used in comparison with the measured cloud properties. Section 4 compares measured and theoretical determinations of cloud radiative properties. Section 5 summarizes the results.

2. Data Sources

Clouds are examined using three primary data types, radiometry from the Landsat-5 satellite and the NASA ER-2 aircraft, lidar from the ER-2, and in situ microphysical measurements from the NCAR King Air and Sabreliner aircraft.

a. *Landsat and ER-2 Radiometry*

Figure 1 gives the location of the Landsat-5 scene used for the present analysis. The dashed line rectangle shows the location of the full scene

image (185 km by 170 km in size), and the solid line rectangle shows the location of the 58.4 km subsection of the image used for the present analysis. This subsection is chosen to maximize coincidence with the aircraft flight tracks, to minimize clear-sky reflectance variations (i.e., use data over Lake Michigan), and to minimize the total data volume.

The Landsat area of interest is shown in Fig. 2 using the Landsat measured brightness temperature for the wavelength region 10.4-12.5μm. The region shown is 512 by 512 pixels with a length of 58.4 km on a side. Each pixel measurement covers a nominal ground area of 114 by 114 meters. Spatial resolution for Landsat solar reflectance bands is 28.5 meters, or 2048 by 2048 pixels. Time of the Landsat overpass is 15:53:12 UTC on October 28, 1986. The satellite takes 8 seconds to acquire data over the 58.4 km region. The Landsat satellite altitude is 920 km and the viewing zenith angles for the area of interest are within 5° of nadir. Solar zenith angle is 63°.

Calibration for all Landsat spectral radiances is taken from Markham and Barker (1986). Four spectral bands are used in the present study. The three solar reflectance bands are 0.76 - 0.90μm, 1.55 - 1.75μm, and 2.08 - 2.35μm. The thermal infrared spectral band covers 10.4 - 12.5μm. The spectral bands will be referred to by the central wavelength of the band, 0.83, 1.65, 2.21, and 11.5μm. Absolute accuracy of solar reflectance bands is estimated as 10% of any radiance value (i.e., 10% uncertainty in instrument gain, Slater et al., 1987). Precision is less than 2 digital counts which is approximately equal to a nadir reflectance change of 0.01 for the present study. Absolute accuracy of the thermal infrared channel is estimated as less than 2K at a radiating temperature of 280K. Precision is 1 digital count (approximately 0.5K for a 280K source and 0.8K for a 240K

source). Calibration of the Landsat sensors is maintained using onboard blackbodies for the thermal infrared and lamps for the solar reflectance channels.

The ER-2 Daedelus scanning radiometer scans 42.65° left and right of the aircraft track. The aircraft altitude is 19.1 km and nominal field of view is 5 milliradians, or about 100 meters on the ground. The three solid lines in Fig. 2 give the location in the Landsat image of the Daedelus data between 15:50:47 and 15:55:32 UTC. The center line is nadir viewing, and the two flanking lines are for a viewing zenith angle of 30° to the left and right of the aircraft. The aircraft flight track was chosen so that the Daedelus scan plane coincided with the solar plane. In this case, the scan to the right of the aircraft (lower line in Fig. 2) is forward scattered radiation (ϕ = 0°) from the cloud and surface, while the scan to the left of the aircraft is backscattered radiation (ϕ = 180°). This orientation was chosen to maximize the sensitivity to anisotropy in the cloud radiation field when comparing simultaneous nadir Landsat reflectance with off-nadir ER-2 Daedelus reflectance. Figure 3 gives a diagram of the Landsat and ER-2 viewing geometry.

Calibration of the ER-2 Daedelus radiometer is accomplished using an integrating sphere on the ground for the solar spectral channels. The present study uses the solar reflectance channel at 0.76μm - 0.90μm. Absolute accuracy of solar channel calibrations is estimated as 10%.

b. *Landsat/Aircraft Navigation*

Nominal navigation accuracy for Landsat and aircraft is 1 km. The aircraft flight track locations and times within the Landsat image are given in Fig. 2. The altitude of the ER-2 flight track is 19.1 km MSL.

Hereafter, all altitudes are given as above mean sea level. The altitude of the King Air flight track ranges from 7.3 km to 7.0 km. The altitude of the Sabreliner flight track is 11.3 km.

The Landsat overpass time is chosen as the reference time for intercomparisons. The aircraft observations are adjusted so that the aircraft measurement of the cloud coincides with the position of the cloud in the Landsat image at 15:53:12 UTC. The flight tracks shown in Fig. 2 include this adjustment.

For the King Air and Sabreliner flight tracks, the cloud is assumed to move with the wind speed and direction at the aircraft altitude. The King Air flew at an altitude of 7.3 km from 15:36:00 to 15:47:20. The aircraft then descended to an altitude of 7.0 km, leveling out at 15:49:15. The King Air remained at 7.0 km through 15:52:00 UTC. Wind speed and direction for the King Air varied from 16.8 m sec^{-1}, 266.4° at 15:36 UTC to 17.1 m sec^{-1}, 263.5° at 15:52 UTC. The resulting cloud motion ranges from 17.3 km (i.e., 16.8 m sec^{-1} × 1032 sec = 17338 m) for the 1536 UTC King Air data to 1.2 km (i.e. 17.1 × 72 = 1231 m) for 1552 UTC data. Note in Fig. 2 that an aircraft contrail parallels the King Air track, about 6 km to the east. The contrail suggests a possible error in the navigation of the King Air track. Comparisons of two independent navigation systems on the King Air (INS and Loran) agreed within 1 km. Given correct navigation, a wind speed of 22.3 m sec^{-1} would be required to move the King Air position to coincide with the contrail. The highest wind speed observed by the King Air at 7.3 km (1536 to 1547 UTC) was 18.7 m sec^{-1}. The average wind speed was 17.0 m sec^{-1}, with a standard deviation of 0.9 m sec^{-1}. Rawinsonde winds at Green Bay (70 km to the west of the Landsat image) ranged from 16.4 m sec^{-1} at 1500 UTC to

19.0 m sec^{-1} at 1800 UTC. We conclude that the contrail visible in Fig. 2 is unlikely to have come from the King Air.

The Sabreliner altitude within the Landsat image was 11.3 km. Wind speed and direction for the Sabreliner varied from 23.9 m sec^{-1}, 266.4° at 15:48:10 UTC to 21.9 m sec^{-1}, 256.3° at 15:53:15 UTC. The resulting cloud motion ranges from 7.2 km for the 15:48:10 Sabreliner data to 0.1 km for the 15:53:15 data.

Navigation of the ER-2 radiometry data into the Landsat image is accomplished in three steps. First, the cloud level which dominates the radiation fields is determined in order to select the appropriate wind speed and direction for cloud movement. Studies of the nadir looking ER-2 lidar (Spinhirne and Hart, 1989) indicate that two cloud layers are present for the Landsat area. The largest optical depths occur for the lower cloud layer at 7-8 km. The cirrus at 9-11.6 km are optically thin.

Second, wind data are obtained using the King Air winds measured at 7.3 km altitude at times of 15:38 UTC and 15:45 UTC where the King Air aircraft intersects the ER-2 flight track. The average wind speed for these two times is 16.6 m sec^{-1} at 268.7° and is similar to winds measured along the entire flight track. In this case, the maximum cloud motion during the time between the ER-2 and Landsat observations (less than 2.5 minutes) is 2.5 km for observations near the beginning and end of the ER-2 track. A comparison of these winds is made with values from the Green Bay rawinsonde data. Wind observations taken from the 1500 UTC and 1800 UTC Green Bay rawinsondes indicate that the vertical variation of wind speed and direction is less than ± 2 m sec^{-1} and ± 5° between 7 and 10.5 km. Time variation of the winds at these altitudes is less than 5 m sec^{-1} and 30° between 1500 and 1800 UTC. Interpolation of the Green Bay winds to the King Air observation

time agrees well with the King Air observed winds. We conclude that uncertainties in the wind speed and direction using the King Air measured values at 7.3 km are small (worst case less than 500 meters uncertainty in cloud movement.

Note that the wind correction of the ER-2 image is not a simple navigation offset, but a compression and rotation of the ER-2 image relative to the Landsat cloud image. The westernmost ER-2 data are remapped toward the east, while the easternmost ER-2 data are remapped toward the west, thereby compressing the size of the ER-2 image by 5/60 or about 8.3%.

Third, the ER-2 cloud image and the Landsat cloud image are correlated for a range of north-south and east-west navigation offsets. A navigation offset of 1.4 km gives the best match of the resulting images. This offset is within the expected aircraft/satellite navigation uncertainty of $(1+1)^{1/2}$ = 1.4 km.

c. *ER-2 Lidar Observations*

The ER-2 aircraft obtained data during the Landsat overpass from a downward pointing lidar (Spinhirne and Hart, 1989). For the present study, three observations of the lidar are useful. First, the radiatively dominant cloud layer is at an altitude of 7-8 km. The optically thick cloud (i.e., temperatures of 240K or less at the beginning of the ER-2 track in Fig. 2) is contained in this 7-8 km layer. Second, an optically thin cirrus layer is present at 9-11.6 km in altitude. Third, lidar depolarization ratios indicate that both layers are composed of ice crystals, except in 100 to 200 meter thick layers of mixed phase ice and liquid water particles found at altitudes between 7.3 and 8.0 km.

Choosing an appropriate cloud type for this lower cloud layer is problematic. The lower cloud layer has characteristics of both cirrus and altocumulus. The cloud layer is composed of predominantly ice particles at an altitude greater than 7 km, the usual boundary between middle and high cloud types. At the same time, some sections of the cloud layer are dominated by water droplets and show cellular features in the Landsat image, typical of altocumulus. Ground observers at Green Bay (1500 UTC) reported the presence of both altocumulus and cirrus. This cloud layer is probably best thought of as a glaciated altocumulus cloud or "cirriform altocumulus" (Starr and Wylie, 1989). The present paper will simply distinguish the two cloud layers present on October 28 as upper and lower. A description of the meteorological conditions can be found in Starr and Wylie, 1989.

d. *King Air and Sabreliner Microphysical Data*

King Air and Sabreliner microphysical data were analyzed to provide information on particle phase and habits (shapes), sizes, and liquid and ice water contents. King Air measurements were taken from the lower cloud layer and Sabreliner measurements were taken from the upper cloud layer.

Particle Measuring Systems 2D-C and 2D-P data were carefully examined to obtain habit information, using direct collections of particles on oil-coated slides (on this and other flights of the King Air) as a reference (Fig. 4). Figure 4a shows a slide collected by the King Air at an altitude of 7.0 km at 15:52 UTC within 1 minute of the Landsat overpass. The figure shows a columnar crystal (top center), spatial plate broken up upon impact (left center), and bullet cluster also broken upon impact (lower center to right). The 2D probes provided data for sizes from 25 microns to above 0.3 cm, but concentrations below about 100 microns are of questionable accuracy

(Heymsfield and Baumgardner, 1985). Ice water content (IWC) was obtained from the particle spectra using "generic" relationships to convert particle dimension to mass, using the appropriate fraction of particles of each observed habit (see Heymsfield, 1977). The IWC is accurate to within a factor of 2 or 3.

Liquid water was detected and water content measured (for LWC > 0.002 g m^{-3}) using a Rosemount icing detector (Heymsfield and Miloshevich, 1989). The icing detector is calibrated using data obtained from the particle collections and a forward scattering spectrometer probe (FSSP). A slide collection taken at 15:38:30 UTC several minutes before the Landsat satellite overpass indicates water droplets (Fig. 4b). The water droplets in this figure might be oversized because of the collection procedure. Droplet size distributions were derived from the FSSP data. Artifacts produced by ice particles are removed using the procedure of Heymsfield and Miloshevich (1989).

Particles larger than 200 microns imaged by the King Air probes were primarily "compact" spherical particles and "compact" spherical particles with extensions. These relatively dense and polycrystalline particles are comprised of bullet and plate-like crystal components (e.g., Fig. 4a) attached to a common center. Bullet rosette particles, which are lower density polycrystalline forms which join at a common center, generally accounted for less than 20% of the crystal population at these sizes, as did columns and plate crystals. Columnar crystals often predominated at sizes between 50 and 200 microns. The slide collections show that most particles below 50 microns were approximately spherical or isometric ice particles. Particles imaged by the Sabreliner probes were primarily columns and compact spherical bullet rosette particles at the lower levels.

Ice water content from the King Air (Fig. 5a) showed considerable horizontal variability, and liquid water was detected (Fig. 5b) at times when IWC were low. Mean droplet diameters (Fig. 5c) were about 8 microns. Median mass weighted ice particle diameters (DBARM) in the King Air data (Fig. 5d) ranged from 300 to 700 microns.

The Sabreliner sampled the upper cloud layer from cloud base to nearly cloud top. This layer was evidently in an active growth stage. Ice water content (Fig. 6a) showed a steady increase with decreasing altitude, except near the lowest level sampled (near a cloud base). Horizontal variability as indicated by the 1-sigma bounds in the data was not as large as for the lower cloud layer. Liquid water was not detected during the Sabreliner cloud penetrations. Changes in DBARM mirrored those for IWC (Fig. 6b). Heymsfield et al (1989) indicate that the IWC are underestimated by as much as a factor of 2 at the upper two Sabreliner penetration levels.

3. Radiative Transfer Theory

The upwelling radiance field is calculated using the Finite Difference Method (Barkstrom, 1976; Suttles, 1981) to solve the radiative transfer equation. Radiance and flux results from the Finite Difference (FD) method have been shown to be in good agreement with results from other radiative transfer methods over a range of optical depths, single scattering albedos, solar zenith angles, and wavelengths (Suttles, 1985). The standard approach is applied to account for azimuth angle variations; a Fourier expansion in azimuth for the radiance and a Legendre expansion in scattering angle for the phase function.

For the present calculations of reflected solar radiation, an isolated cloud is considered. Atmosphere above and below the cloud is neglected. The surface below the cloud layer is assumed to be non-reflecting. Depending on the optical depth, 50-100 depth points are used. In all cases, 15 zenith angle points are used on the interval 0 to 90 degrees. The Fourier and Legendre expansions included 72 to 120 terms based on the phase function being used. Solar irradiance data were taken from values recommended by the World Radiation Center in Davos, Switzerland (Iqbal, 1983). Cloud optical inputs required are physical thickness, scattering and absorption coefficients, and phase function. The cloud physical thickness is adjusted to achieve a desired extinction optical depth. The scattering and absorption coefficients have been based on Mie scattering calculations.

Phase function information is taken from several sources: Henyey-Greenstein analytic form, Mie calculations, and experimental observations by Volkovitskiy, Pavlova, and Petrushin (1980), hereafter denoted VPP. The strong forward scattering peak of the VPP phase function (Foot, 1988) is treated using the delta function approximation of Potter (1970).

For comparison to the Landsat spectral radiance measurements, calculations are performed at a total of 23 wavelengths. The Landsat band 4 (0.76-0.90μm) is modeled using a wavelength of 0.83μm. This channel is an atmospheric window with essentially conservative scattering, similar to the visible wavelength channels typical of meteorological satellites. Band 4 is used in the present study because of its large dynamic range, allowing unsaturated reflectance measurements even for large optical depth clouds. Since the clouds are at altitudes of 7 km or greater and temperatures of 240K or colder, water vapor absorption is neglected. The Landsat band 5

(1.55-1.75μm) and band 7 (2.08-2.35μm) are atmospheric window channels with moderate absorption by liquid water and ice. These spectral regions have been employed by several studies to remotely sense cloud particle size, since the amount of cloud absorption depends on the path length of radiation through the particle (Curran and Wu, 1982; Twomey and Cocks, 1982; Wu, 1985; Foot, 1988). The imaginary index of ice varies by a factor of 3-4 within these spectral bands, so that calculations using a single wavelength (using a band averaged imaginary index) gave errors for inferred cloud particle size (section 4.c) of up to 30% relative to calculations using 11 wavelengths. The present calculations use 11 wavelengths which are then weighted by the Landsat spectral response function (Markham and Barker, 1985) to provide a final band averaged spectral radiance. Index of refraction values for ice are obtained from Warren (1984). Values for water are obtained from Palmer and Williams (1974) for bands 4 and 5, and from Downing and Williams (1975) for band 7.

4. Theory vs. Observations

Observations will be compared to theoretical radiative transfer calculations for three specific cases. Each case highlights different aspects of the cloud radiative properties. The first case is a comparison of 0.83μm nadir reflectance versus 11.5μm emittance. This relationship is critical to the derivation of cirrus cloud height using bispectral satellite imagery as in ISCCP. The second case is a comparison of theoretical and measured anisotropy of cloud reflectance at 0.83μm. The reflectance of cloud fields is expected to be non-Lambertian. Anisotropic cloud scattering can result from either non plane-parallel cloud geometry (Davies, 1984) or

from anisotropic cloud particle scattering. Optically thick clouds are expected to be sensitive to cloud shape. Optically thin clouds are expected to be sensitive to the form of the particle scattering phase function. Particle scattering phase functions for cirrus are currently uncertain due to both the difficulty of modeling non-spherical particles and the variability of observed particle shapes. The third case is a comparison of nadir reflectance at 0.83, 1.65, and 2.21μm wavelengths. This last case tests the ability to remotely sense cloud particle size with space borne radiometers. Radiatively determined cloud particle sizes are compared to in situ measurements from the King Air aircraft.

a. *0.83μm Nadir Reflectance vs. 11.5μm Emittance*

Figure 7 gives the observed nadir reflectance R versus 11.5μm effective emittance ϵ_e using the Landsat radiances along the ER-2 groundtrack (data shown as circles). Figure 2 gave an image of the ER-2 groundtrack in the Landsat scene for the 11.5μm data. Figure 8 gives the same image for the Landsat 0.83μm reflectance. The calculations performed to produce Fig. 7 are given below.

i. Landsat Observations

Nadir reflectance is calculated as an equivalent Lambertian reflectance,

$$R = \pi L / (S_0 \cos\theta_0), \qquad (1)$$

where L is spectral radiance ($Wm^{-2}sr^{-1}\mu m^{-1}$), S_0 is solar spectral flux ($Wm^{-2}\mu m^{-1}$) averaged over the narrow spectral bandpass (Markham and Barker, 1986), and θ_0 is the solar zenith angle (63°).

In order to make the model and measurements more directly comparable, the first order reflectance of the surface (Lake Michigan) has been removed as described in Platt et al. (1980). This correction accounts for surface reflectance of the direct solar beam transmitted through an optically thin cirrus, and for radiation diffusely scattered down from the cirrus to the surface and then reflected back to the satellite. The correction causes the data to tend to zero reflectance and zero emittance as cloud optical depth tends to zero. The magnitude of the surface reflectance correction is approximately 0.04 in nadir reflectance for small optical depths, decreasing to no correction for large optical depths.

Effective emittance is calculated following Platt et al. (1980),

$$\epsilon_e = (L_{clr} - L_m)/(L_{clr} - L_{cld}) \qquad (2)$$

where L_m is the measured 11.5μm radiance, L_{clr} is the clear-sky 11.5μm radiance determined using the apparently clear area in the lower right of Figure 2 with a brightness temperature of 280.0 K, and L_{cld} is the blackbody radiance which would be emitted by an optically thick cloud at the altitude of the cirrus layer. Cloud altitude is determined based on the ER-2 lidar data and the ER-2/Landsat stereo cloud heights. The average effective cloud height is chosen at 8.5 km, between the upper and lower cloud layers, but closer to the optically thicker lower layer. For true cloud heights of 7.5 or 10 km (near center of lower and upper cloud layers), the uncertainty in calculated emittance is ± 15% of any emittance value. The cloud temperature of 236.3K at an altitude of 8.5 km is taken from the Green Bay radiosonde at 1500 UTC.

ii. Theoretical Calculations

Multiple scattering calculations are performed using the Finite Difference (FD) method as discussed in section 3. Calculations produce upwelling radiances as a function of viewing angle for a solar zenith angle of 60°. A range of phase functions and optical depths are used at a wavelength of 0.83μm. Calculated radiances are converted to reflectance in the same manner as the Landsat data.

For 11.5μm radiation, the calculated beam absorption emittance is given by

$$\epsilon_a = 1 - e^{-\delta_a} \qquad (3)$$

where δ_a is the absorption optical depth at 11.5μm. For cases using Mie phase functions, the absorption optical depth is determined using the Mie calculations at 11.5μm. For cases using the Henyey-Greenstein or VPP phase functions, $\delta_a = \delta_e/\alpha$, where δ_e is the extinction optical depth at 0.83μm and $\alpha = 2.0$. This relationship requires that the particle radius be much greater than the wavelength, in this case 11.5μm (see van de Hulst, 1957). In particular, this large particle limit specifies that the particle extinction efficiency Q_{ext} is 2.0 at 0.83μm and the particle absorption efficiency Q_{abs} is nearly 1.0 at 11.5μm. This assumption should be accurate for polydisperse particle distributions with radius greater than 30μm. Platt et al. (1987) found theoretical values of α between 1.85 and 2.15 for ice spheres and ice cylinders with a radius of 30μm or greater. Measured values of α, however, ranged from 3.0 to 5.5 using lidar backscatter and uplooking 11μm radiometer data taken from the ground (Platt et al., 1987). As particle size decreases, the absorption efficiency at 11.5μm decreases

and α increases. For a Mie phase function with mode radius of 3.8μm, α = 3.4.

iii. Discussion

The results in Fig. 7 compare the measured relationship of nadir reflectance and effective beam emittance with the model relationship of nadir reflectance and absorption beam emittance. Henyey-Greenstein phase functions are used with asymmetry parameter values g of 0.5, 0.7, and 0.86. The theoretical calculations use α = 2. A value of g = 0.86 is typically used to represent scattering from water droplet clouds, and g = 0.7 is more typical of scattering from large cylindrical particles (Platt and Stephens, 1980). As g increases, particle scattering is increasingly dominated by forward scattered radiation. A value of g = 0 indicates isotropic scattering, while g = 1.0 indicates complete forward scatter. An initial conclusion based on Fig. 7 is that the cirrus scattering is more consistent with cylindrical scattering than with spherical scattering, as suggested by Platt et al. (1980).

While the agreement in Fig. 7 with g = 0.7 is very gratifying, the agreement is fortuitous. First, we noted in section 2.d that small water droplets dominated the King Air microphysical measurements at location 1 in Fig. 8. This portion of the cloud field is included in the data given in Fig. 7, but we find no difference between the water droplets and large ice crystal portions of the cloud field. Second, King (1987) has shown that calculations of cloud radiative properties based on radiance measurements (as performed here) are much more sensitive to the scattering phase function shape than flux calculations. Figure 9 gives more precise model

calculations for comparison with the Landsat observed cloud field properties.

Figure 9 gives three comparisons with the data, all calculated using the FD method. The data points which correspond to regions dominated by small water droplets in the King Air data are shown as solid circles. As mentioned, the water droplet data fall within the range of scatter of the larger ice particle results in Fig. 9.

The first model calculation uses a Mie scattering phase function and Mie extinction and absorption cross-sections at 0.83μm. The results use the FSSP microphysical data from the King Air, with an effective radius r_e of 3.8μm. Effective radius r_e is given by

$$r_e = \frac{\int N(r)\, r^3\, dr}{\int N(r)\, r^2\, dr} \qquad (4)$$

where N(r) is the cloud particle number density (Number $m^{-3}\mu m^{-1}$). Mie calculations at 8 wavelengths in the Landsat 10.5μm channel bandpass are used to determine $\alpha = 3.45$ for this size distribution. The FD calculations of nadir reflectance and ϵ_a are given as the short dashed curve in Fig. 9 and agree well with the observations dominated by small water droplets (filled circles).

If we use the large particle assumption of α=2 with the Mie phase function, we obtain the result given by the long dashed line in Fig. 9, in poor agreement with the data. This points out the importance of particle size in the determination of α for particles less than about 30μm, and its effect on the reflectance/emittance relationship.

We now see that the similarity between the reflectance/emittance relationships in Fig. 9 for ice and liquid water particles is fortuitous. An increase in particle size would move the water droplet results toward the long dashed line for two reasons: first by decreasing α, as seen in Fig. 9 and second by increasing g (i.e., more forward scatter) as seen in Fig. 7. We conclude that the reflectance/emittance relationship is fundamentally dependent on two parameters: the scattering phase function and the value of α. Both of these parameters are a function of particle size, and their effects for the Mie scattering case are additive.

Why then, given the large range of particle size observed by the King Air (and Sabreliner), are the ice data (open circles) giving such small scatter in the data? One reason is that the ice particle distributions measured by the King Air were significantly larger than 30μm, so that α=2, independent of particle size. A second possibility is that the ice scattering phase function is not a strong function of particle size, even though Mie phase functions are a strong function of particle size. This is especially true for the 117° scattering angle appropriate for the nadir Landsat observations examined here. As particle size increases, the Mie scattering phase function magnitude at 117° drops, thereby reducing cloud reflectance for a given cloud optical depth. For reference, ISCCP uses an assumed Mie particle size of 10μm with α=2.704 (Rossow et al., 1985). The ISCCP curve would be closer to the long dashed curve in Fig. 9 and would overestimate cloud emittance for a given nadir reflectance measurement. This in turn would cause an underestimate of true cloud height.

Since the theoretical results in Fig. 9 are sensitive to the phase function, we also examined the laboratory measured ice particle phase function of VPP (Volkovitskiy et al., 1980). The VPP measurements were for

columnar ice crystals 20 to 25μm in length, at a wavelength of 0.63μm. This phase function is given in Fig. 10 along with the Mie phase function for r_e = 3.8μm and the Henyey-Greenstein phase functions with g = 0.5, 0.7, 0.86. The ice phase function (VPP) shows considerable increases in side scattered radiation (near 90°) compared to the water droplet phase function (Mie). While not shown, this difference between the Mie and VPP phase functions increases with increasing droplet size. For the VPP calculations, the particle radius is assumed to be larger than 30μm, so that α=2 is used. Support for this assumption in the lower cloud layer comes from the King Air data which gives ice particle r_e ranging from 100 to 400μm. Satellite derived ice-particle r_e is about 60μm (see section 4c). The VPP phase function gives better results than the small particle Mie phase function, and much better results than Mie phase functions with larger (say 60μm) particle sizes. Even the VPP, however, shows insufficient side scatter to explain the data. Foot (1988) found similar results with the VPP phase function using aircraft radiance measurements above a cirrus cloud with ϵ_a = 0.2. The VPP under-predicted the observed reflectance by 0.013 (Foot, 1988, Fig. 8), similar to our results at the same value of ϵ_a in Fig. 9.

iv. Error Analysis

The primary error source for the Landsat observations used in Figs. 7 and 9 is the determination of an effective cloud height/temperature used in calculating ϵ_e. The two cloud layers present on October 28 complicate the cloud height determination. The resulting range of uncertainty is indicated in Fig. 11. The solid line is a fit through the data, with cloud height assumed at 8.5 km. The results using a cloud height of 7.5 km (center of

the 7-8 km cloud layer) are given by the long dashed line. Results using a cloud height of 10 km (near the center of the upper 9-11.6 km layer) are given by the short dashed line. The uncertainty in emittance is ± 15% of any given emittance value. Figure 11 indicates that much of the scatter in the Landsat observations might be explained by the variability in effective cloud height.

A second error source is the difference between ϵ_e as measured by the satellite, and ϵ_a as determined using theory. In the absence of cloud scattering, these two quantities are identical (Platt et al., 1980). Scattering reduces the surface emitted radiation transmitted through the cloud, causing the cloud to appear colder. As a result, scattering at 11.5μm causes the satellite derived ϵ_e to exceed ϵ_a. The magnitude of $\epsilon_e - \epsilon_a$ depends strongly on the scattering phase function. Wielicki (1980) found values of $\epsilon_e - \epsilon_a$ less than 0.01 using Mie scattering phase functions for ice clouds with r_e = 5, 10 and 20 μm. Platt and Stephens (1980) used cylindrical ice particle phase functions and found values of $\epsilon_e - \epsilon_a$ ranging from 0.03 at ϵ_a = 0.2, to 0.10 at ϵ_a = 0.6. Correction of the Landsat derived values of ϵ_e to ϵ_a using Platt and Stephens (1980) changes the solid line in Fig. 11 to coincide very closely with the short dashed line given for a cloud height of 10 km. Because the lines were so close, only one is plotted in Fig. 11. While this correction is highly uncertain at the present time, we note that this correction would increase the disagreement between the observations and the theory for the VPP phase function given in Fig. 9. The results of Wielicki (1980) for ice and liquid water spheres indicate that the agreement for the small water droplet Mie scattering would remain unchanged in Fig. 9.

We conclude that these uncertainties would not change the overall conclusions reached earlier. Namely, the liquid water cloud results are in agreement with theory. The ice cloud results require either much more side scatter in phase functions (more even than the VPP ice phase function), or an effective particle radius much smaller than 30μm, so that α is much larger than 2. Indeed, if the VPP phase function is assumed correct, and the correction of Platt and Stephens (1980) is applied to adjust the Landsat ϵ_e to ϵ_a, then a value α of about 4 would be required for agreement between theory and data, implying a particle size less than 4μm. Estimates of particle size from other cloud radiative properties in section 4c indicate an effective ice particle radius of about 60μm. Lidar backscatter estimates (Spinhirne and Hart, 1989) give 20μm for the upper cirrus layer. Microphysical data in the lower cloud layer (King Air) gives an effective radius of about 200μm. We conclude that the differences found in Fig. 9 are probably caused by errors in the phase function. The observations require larger amounts of side scatter (near 90° scattering angle) than is found in the VPP phase function. Unfortunately, other estimates of ice particle phase functions (Coleman and Liou, 1981; Sassen and Liou, 1979) give even less side scatter than the VPP experimental results (Foot, 1988). This enhancement of side scatter may be caused by multi-faceted cloud particles (assemblages of plates) such as those found to predominate in the King Air microphysical data.

b. *Reflectance vs. Viewing Zenith Angle*

A second test of theoretical calculations is their ability to predict the reflectance anisotropy as a function of viewing zenith angle and viewing azimuth angle. A particularly useful test is the determination of the ratio

of reflectance viewing the same cloud at two different angles. This ratio eliminates sensitivity to uncertainties in the absolute gain calibration of the radiometers. The ER-2 scanning radiometer data was used to provide observations as a function of angle in the solar plane (i.e., viewing azimuth angle of 0° (forward scatter) while scanning to the right of the aircraft, and 180° (backward scatter) while scanning to the left of the aircraft). Figure 3 gives a schematic of the geometry for the Landsat/ER-2 intercomparison.

The first step in this process is to use the nadir ER-2 observations to intercalibrate the ER-2 Daedelus and Landsat radiometers for radiation at 0.83μm (0.76-0.90μm). After navigation, a regression of 1-km averaged ER-2 and Landsat radiances gave R(ER-2) = 0.759*R(Landsat) - 1.42 (units of nadir reflectance) with a 2σ uncertainty in the gain of ± .020 and correlation coefficient of 0.995. The final intercalibrated reflectances are given in Fig. 12.

While the final agreement between the radiometers is good, the relative gain differences in these two radiometers at 0.83μm are larger than expected. Because of this discrepancy, comparisons of the AVHRR integrating sphere used to calibrate the Daedelus radiometer were made with a sphere and hemisphere at NASA Goddard Space Flight Center. Tests indicated that the AVHRR sphere calibration was low by about 28%, which would give good agreement between the ER-2 and Landsat radiometers. More careful calibrations of narrowband radiometers are recommended for future work. The present work uses the Landsat radiances as the standard.

Having navigated and intercalibrated the Landsat and ER-2 radiometer data at nadir, off-nadir observations at 30° were examined. In view of the presence of two cloud layers and lack of lidar data for off nadir viewing,

the 30° viewing zenith angle data were navigated using test cloud altitudes between 6.5 and 12.5 km. Spatial variations in the 30° viewing zenith ER-2 data most closely matched those in the nadir Landsat view when cloud height was set to 8.5 km, slightly above the top of the lower cloud layer at 7-8 km. Poor correlations were found assuming cloud heights within the upper cloud layer. This stereo cloud height test indicates that the shortwave radiative properties are dominated by the lower cloud level, consistent with microphysical measurements showing decreasing ice water content with increasing cloud height (Fig. 6a) and with the lidar backscatter intensities (Spinhirne and Hart, 1989).

After subtracting the surface reflectance contribution as in section 4a, measured cloud reflectance ratios are given in Fig. 13. The cloud reflectance ratio for forward scattered radiation $R(\theta=30,\phi=0)/R(\theta=0)$ is given in Fig. 13a and ranges from 1.0 to 2.2 with a mean value of 1.60. The reflectance ratio for backward scattered radiation $R(\theta=30,\phi=180)/R(\theta=0)$ is given in Fig. 13b and ranges from 0.6 to 1.3 with a mean value of 0.97.

Theoretical calculations for the reflectance ratios using the FD model discussed in section 3 are also given in Fig. 13 for comparison. Results are given using the VPP phase function, the Mie phase function ($r_e = 3.8\mu m$), and for a Henyey-Greenstein phase function with $g = 0.7$. The results for forward scattered radiation (Fig. 13a) are consistent with any of the three phase functions. The results for backward scattered radiation (Fig. 13b) are consistent with the VPP and Henyey-Greenstein phase functions, but are in poor agreement with the water droplet phase function. Foot (1988) also found good agreement with the VPP phase function for multiple angle views of a cirrus cloud at 11.3 km altitude over Ireland in March 1981. Radiometer

measurements were taken from an aircraft banked at 30° over a horizontally homogeneous cirrus layer.

The primary information contained in the reflectance ratios is a ratio of the magnitude of the phase function at the two scattering angles being examined. Indeed for the case of optically thin single scattered radiation, the reflectance ratio is directly proportional to the phase function ratio (Buglia, 1986). For multiple scattered radiation the relationship is not as simply defined. Recall from Fig. 10 and the geometry shown in Fig. 3 that the viewing angles considered in this section correspond to the following scattering angles in the phase function: nadir is 117° scattering angle, backscatter at 30° viewing zenith is a scattering angle of 147°, and forward scatter at 30° viewing zenith is a scattering angle of 87°.

A knowledge of the scattering angle and the phase function simplifies an understanding of the theoretical predictions in Fig. 13. For example, the backscatter ratio predicted for water droplets is very large at small optical depths (i.e., small nadir reflectance). Examination of the phase function shows that the 147° scattering angle is in the "rainbow" peak of the phase function, while the 117° scattering angle is at the minimum of the water droplet phase function. In this case, the water droplet phase function predicts a large reflectance ratio, while the VPP and Henyey-Greenstein phase functions have similar magnitudes at these two angles, predicting smaller reflectance ratios. Of course, as the optical depth increases, multiple scattering will reduce the effect of the phase function, and reflectance ratios for water droplets are closer to 1. This indicates that optically thin cirrus observations using multiple angles of view can give information concerning the relative magnitude of the phase function (but not its absolute magnitude) at the angles considered.

Uncertainties in the above calculations include:

i. Specification of cloud altitude. An incorrect specification of cloud altitude will cause an error in alignment of the ER-2 and Landsat cloud observations. The two radiometers will not view the same portion of the cloud field. A related difficulty is the finite thickness of the cloud layer (or layers in the present case). Even for a single cloud layer with known altitude, the off-nadir view and nadir view will only view radiation from exactly the same cloud particles in the limit of an infinitesimally thin cloud. For finite cloud thickness, horizontal inhomogeneities in the cloud field will add noise to the reflectance ratios. An estimate of the magnitude of these two error sources is given in Fig. 14. Figure 14 gives the backscatter reflectance ratio for three assumed cloud heights: 7.5, 8.5 and 9.5 km. A 1-km change in cloud height shifts the horizontal position of the Landsat data selected to match the ER-2 by (tan 30°)(1000m) = 577 meters. The resulting variability in Fig. 14 is about ± 0.1, much less than the differences distinguished in Fig. 13 between the Mie phase functions and the VPP. For a horizontally homogeneous cloud field, we would find no variability with assumed cloud height.

ii. Surface Reflectance Correction. For very thin cirrus, the correction for the surface reflectance (about 0.04 for $R(\theta=0)$) approaches the magnitude of the cloud reflectance. In this case, even small errors in this correction due to varying atmosphere (i.e., aerosols) and surface (i.e., wave state and turbidity) conditions can cause relatively large errors in the anisotropic ratio. The magnitude of these errors is currently unknown.

iii. Horizontal Cloud Variability. The forward and backscattered ER-2 measurements view different parts of the cloud field (i.e., left versus right side of the aircraft track). Horizontal variations in particle

scattering might give inconsistent results. This possibility is tested by examining the Landsat nadir viewing cloud properties at the two off-nadir ER-2 viewing positions. The reflectance/emittance relationships (section 4a) and the inferred cloud particle size (section 4c) were found to be similar at the ER-2 off-nadir positions.

c. *Visible vs. Near-Infrared Nadir Reflectance*

Theoretical calculations predict that cloud reflectance in near-infrared windows such as those at 1.6μm and 2.2μm should give lower reflectances than at visible wavelengths (Pollack et al., 1978; Hansen and Pollack,1970; Twomey, 1971). The reason for this difference is that ice and liquid water show significant absorption at these wavelengths, in contrast to the nearly conservative scattering at wavelengths shorter than 1μm. In addition, because the amount of absorption scales with the path length of radiation through the particle, increasing cloud particle size should lead to decreasing reflectances at 1.6μm and 2.2μm. Measurements at these wavelengths to date, however, have often given unpredicted results. Twomey and Cocks (1982) found unexpectedly high absorption (factors of 3 to 5) in optically thick liquid water clouds. Curran and Wu (1982) found unexpectedly low absorption in optically thick high clouds, and postulated the existence of supercooled small water droplets in place of the expected large ice particles. We will examine the implications of the FIRE data for optically thin cirrus.

The Landsat satellite has spectral bands at 0.83μm, 1.65μm, and 2.21μm which cover this range of variation in cloud absorption. Figure 15 gives the ratio R(2.21μm)/R(0.83μm) for the nadir Landsat data. These data cover the same region as shown in Fig. 2. At 15:38:30 UTC the King Air aircraft

took a direct sample of the cloud particles on an oil covered slide. The sample is shown in Fig. 4b and is dominated by water droplets with a mean radius of about 4μm. This sample corresponds to a reflectance ratio of about 0.75 found in the Landsat data at location "1" in Fig. 15. There is a time difference of 15 minutes between the King Air and Landsat observations. The liquid water regions of this cloud, however, appear to have been colloidally stable (Heymsfield et al, 1989). A second direct cloud particle sample was collected at 15:52 UTC. This sample is shown in Fig. 4a and contains only ice particles (broken spatial plates and some columns, 20 to 300μm in length). This second sample corresponds to a reflectance ratio of about 0.4 found in the Landsat data at location "2" in Fig. 15. Note that the reflectances used to derive the image in Fig. 1 are not corrected for surface reflectance. In this case the reflectance ratios are a mixture of clear and cloudy signatures.

Given this qualitative agreement between the satellite and aircraft data, the next step is to test the quantitative agreement along the King Air aircraft track. The Landsat radiance data are spatially averaged to 1 km resolution, sampled every 0.5 km along the King Air groundtrack. Cloud reflectances are then corrected for surface reflectance effects as in section 4a. The 1.65μm and 2.21μm channels are found to require less than 0.01 correction for surface reflectance.

Figure 16 compares theoretical calculations using the FD method with the measured nadir cloud reflectance at 0.83μm and at both 1.65μm and 2.21μm along the King Air groundtrack. Calculations use a solar zenith angle of 60°. The VPP phase function is used for calculations with ice particles, while the 3.8μm radius Mie phase function is used for calculations with water droplets. Figures 16a and b give results for 1.65μm. Figures 16c and

16d give results for 2.21μm. The Landsat data are shown with symbols indicating the corresponding portion of the King Air track shown in Fig. 15.

It is evident that there are two distinct populations of cloud particles along the 88 km track. The high reflectance ratio values in Fig. 15 (15:38:10-15:39:09 UTC and 15:49:40-15:50:39 UTC) appear along the diagonal of nearly equal reflectance at the two wavelengths and are consistent with water droplets or ice spheres with radius less than 7.5μm. The remaining data indicate larger particles of about 60μm radius. Examination of the 1.65μm versus 2.21μm data given in Fig. 16 indicates that the large particles are ice. An assumption of liquid water for the large particles would give inconsistent particle sizes at 1.65 and 2.21μm. An assumption of ice gives consistent particle size in the two wavelengths. The small particles are too small to reliably distinguish ice from liquid water phase for these optically thin clouds.

Figure 17 gives the King Air particle size distributions using the combined FSSP, 2D-C, and 2D-P probes. For the 2D-C and 2D-P probes, particle size is calculated as a sphere with cross-section area πr^2 equal to the area of the particle image in the 2-D probe. For compact non-spherical particles, this specification is similar to using equivalent volume spheres (Pollack and Cuzzi, 1980). Pollack and Cuzzi (1980) found that for large size parameter $x = 2\pi r/\lambda \gg 1$, and moderate absorption $2n'x < 1$) (where n' is the imaginary index of refraction), equivalent volume spheres are most accurate for absorption efficiency determination. For the 1.65μm and 2.21μm spectral bands, the appropriate radius range would be from about 3μm to 400μm. Given the compact particle habits observed in the microphysical data, the use of equivalent cross-section area spheres should be reasonably accurate. Large aspect ratio particles would lead to an

overestimate of the true particle volume, and therefore an overestimate in particle absorption at 1.65 and 2.21μm. Such particles, however, were rarely noted in the data.

Four characteristic size distributions are given in Fig. 17. The data for 15:38:10 to 15:39:09 UTC cover the high ratio of R(2.21)/R(0.83) found in Fig. 15 near the location "1" in the figure (i.e. colored red in the image). The microphysical data are dominated by small water droplets with radius about 4μm. The next section of the flight track (15:39:10 to 15:45:24 UTC) shows a peak at about 150μm, but no water droplets. The third section (15:49:40 to 15:50:39 UTC) has the smallest particle concentrations, and is taken from the high ratio of R(2.21)/R(0.83) found just before the end of the King Air track in the Landsat image. The Landsat data imply small particle sizes, while the aircraft finds no small drops in the FSSP probe. Spinhirne and Hart (1989) noted from the ER-2 lidar data that the mixed phase cloud occurred in vertically thin layers (100 - 200 meters thick) at heights between 7.3 and 8.0 km. The lidar depolarization data at location '1' in Fig. 15 verifies the existence of a mixed ice/liquid water phase cloud layer at 7.3 km altitude (Spinhirne and Hart, 1989), the position of the King Air at 15:38:30 UTC. The King Air altitude at 15:50 UTC is 7.0 km, which is below the lidar detected altitudes for mixed phase cloud. It is likely that the King Air data at 15:50 missed the liquid water layer. We conclude that the aircraft microphysics and Landsat reflectances are in qualitative agreement, subject to uncertainties in the vertical variation of cloud microphysics and temporal evolution of the cloud field.

The quantitative comparison of aircraft and radiometrically derived particle size requires the determination of an effective mean particle radius. Figure 18 gives the Landsat 2.21/0.83μm cloud reflectance ratio

versus effective radius r_e (eq. 4) derived using the King Air microphysics data. This effective radius is a cross-section area weighted radius and has been shown useful in characterizing overall radiative properties of a particle size distribution. The number densities are averages over 5-second intervals, which results in size distributions representative of 500-meter sections of the cloud field.

Figure 18 indicates a significant but poor correlation between aircraft particle size and the 2.21/0.83μm reflectance ratio. There appear to be three clusters of data, one with r_e of about 4μm, and two with r_e about 200μm. The apparently anomalous data with large particle size and large reflectance ratio (15:50 UTC) are the liquid water layer missed by the King Air as discussed above. Recall that the data in Fig. 16 also clustered in two particle size groups, water droplets with radius less than 7.5 micron, and ice particles with radius about 60μm. While the water droplets appear consistent between the two data sources, the ice particles are in substantial disagreement, the radiative measurements indicating a smaller particle size by about a factor of 3. In order to understand this discrepancy, the errors inherent in such a comparison are examined below.

i. Uncertain Index of Refraction; factor of 2.

Warren (1984) estimates that the uncertainty of the imaginary index of refraction for ice in the 1.4 to 2.8μm spectral region is a factor of 2. This uncertainty could result in a factor of 2 error in the particle size inferred from the comparison of measured and theoretically calculated reflectances. This simple relationship between refractive index and inferred particle size can be shown using anomalous diffraction theory, which predicts the particle absorption efficiency to be a function of

(rn'/λ) (van de Hulst, 1957) where r is particle radius, n' is the imaginary refractive index, and λ is wavelength.

ii. Uncertainty in the scattering phase function: ± 30%.

Use of the Mie scattering phase function in place of the VPP gave particle sizes about 60% smaller than those predicted in Fig. 16. This is an extreme test of the phase function sensitivity, and we estimate the true uncertainty relative to the VPP phase function as about half this value.

iii. Uncertainty in the use of a single particle radius to represent an entire size distribution: ± 15% at $r_e < 200\mu m$.

Mie calculations were run to determine single scatter albedo as a function of r_e for the King Air size distributions (5 second averages) for each wavelength. These complete calculations were then compared to Mie calculations using a single particle size (as in Fig. 16). Errors in single scatter albedo can then be converted into an equivalent particle size error. For r_e less than 200μm, these errors induce a scatter in derived particle size of 15% or less. As r_e increases beyond 200μm, an increasing bias error occurs which, at 400μm, would cause particle size inferred using Fig. 16 to underestimate the true value of r_e by 30%. This result confirms the use of r_e as effective particle size for absorption calculations. It can be shown that single scatter albedo is rigorously conserved using a single particle radius of r_e if extinction efficiency $Q_{ext} = 2$ (i.e., $x \gg 1$) and if absorption efficiency Q_{abs} is a linear function of n'r. This latter constraint is approximately true for $2n'x < 1$, where x is size parameter and n' is the imaginary index of refraction. For the 2.21μm channel, this limit is about $r < 400\mu m$. Both constraints are well satisfied for the cirrus case examined.

iv. Uncertainty in converting 2D image area to equivalent sphere: Unknown.

This error is composed of three parts. First, there is a theoretical error in the approximation of non-spherical particles by a spherical shape. Second, there is a measurement error in the determination of the size of a three-dimensional particle using a two-dimensional image. Third, 2-D probes have poor resolution for particles less than 100μm, causing those particles to appear spherical in the 2-D images. All of these errors are topics of current research (e.g. Heymsfield and Platt, 1984; Takano and Liou, 1989). The good agreement between the King Air median mass-weighted diameter determined as a function of crystal habit (Fig. 5d), and 2 r_e determined using particle cross-section area (Fig. 18) argues that this error is of secondary importance.

v. Inadequate microphysical sampling: Unknown.

The size comparisons in Fig. 18 are given using the King Air measurements in the lower cloud layer at 7.3 km. Measurements of the upper cloud layer by the Sabreliner (Fig 6b) show mean particle radius decreasing from 200μm at 9 km to 40μm at 11 km. Note that a 20μm radius is the smallest particle size measured by the 2D-C probe at the Sabreliner airspeed. Many small particles in the upper cloud layer are undoubtedly missed by the 2D-C and 2D-P probes (Heymsfield et al, 1989). Figure 17, shows in addition that small particles are also missed in the lower cloud layer measurements. Figure 17 shows that all of the 2-D size distributions at 7.3 km have maximum number density for the smallest particle size measured by the 2D-C probes. In support of this concern, Spinhirne and Hart (1989) estimate a mode radius of 20μm for the upper cirrus layer on October 28 using integrated lidar backscatter and 11μm emittance. While the effect of these unsampled small ice particles on the determination of r_e is

unknown, it seems reasonable from the size distributions shown in Fig. 17, that this effect alone might explain the discrepancy between 60 and 200μm values for r_e.

vi. Horizontal variations in cloud particle size; Negligible for mean particle size.

The Landsat 1 km averaging circle will not match the 500-meter line of aircraft data. Navigation accuracy of the Landsat/King Air data are 1 km for time coincident data, and may be 2-3 km for data near 1536 UTC. Figure 15, however, indicates that the high reflectance ratio scenes are clustered in two cloud cells along the King Air track with sizes of 5 to 15 km. Given the long track of data used (88 km), it is unlikely that large biases in the particle size comparisons are caused by horizontal spatial sampling errors. These errors will be predominantly random.

5. Conclusions

The FIRE October 28, 1986, data provide a unique opportunity to compare measured and theoretical cloud properties for cirrus clouds. Overall impressions from the present analysis are:

1. The lower cloud layer (7-8 km) appeared to dominate the cloud radiative properties as viewed by the ER-2 and Landsat. This result is consistent with the King Air and Sabreliner microphysical measurements and with ER-2 lidar observations.

2. The cirrus clouds produced more side-scattered radiation (scattering angle 60°-120°) than predicted by spherical particles. Non-spherical particle scattering better describes the cirrus observations, although currently available cylindrical, hexagonal, and laboratory measured ice

particle phase functions still underpredict the amount of side-scattered radiation found in the observations.

3. Multiple angle reflectance measurements in the solar plane were compared to theoretical calculations. Results indicate that the shape of the phase function at scattering angles of 87, 117, and 147 degrees agrees fairly well with the VPP measured phase function and with a Henyey-Greenstein phase function using $g = 0.7$.

4. Particle size inferred using Landsat cloud reflectance at 0.83μm, 1.65μm and 2.21μm gave good agreement with the King Air cloud particle samples for portions of the cloud field dominated by small water droplets with $r_e = 3.8\mu m$. For the larger ice crystals, the radiation measurements determined an r_e of about 60μm, compared to about 200μm determined using the King Air FSSP, 2D-C, and 2D-P probes. We conclude that the discrepancy is caused by two uncertainties. First, ice particle sizes below about 20μm are not detected by the aircraft probes. The particle number densities are maximum at the smallest particles sensed by the 2-D probes, indicating the presence of smaller ice particles, even in the radiatively dominant lower cloud layer at 7-8 km. Second, uncertainties in the imaginary index of ice for the 1.65 and 2.21μm spectral bands causes an uncertainty of a factor of two in the Landsat derived particle size. The effect of small ice particles in the upper cirrus layer at 9-11.6 km is estimated to be of secondary importance.

5. Recommendations for future cirrus experiments include improved measurement of ice particle concentrations for sizes between 1 and 50μm, improved sampling of the vertical variation of cloud microphysics, more accurate radiometric calibration of aircraft radiometers, and more accurate values for the imaginary index of ice between 1.5 and 2.5μm wavelengths.

Acknowledgments: We are indebted to Nancy Knight for collection of the ice particle and droplet samples and to NCAR's Research Aviation Facility for the acquisition of the King Air data.

6. REFERENCES

Barkstrom, B. R., 1976: A finite difference method of solving anisotropic scattering problems. *J. Quant. Spect. Rad. Transf.*, 16, 725-739.

Buglia, J. J., 1986: Introduction to the theory of atmospheric radiative transfer. NASA Reference Publication 1156, July, 1986.

Coleman, R. F., and K-N Liou, 1981: Light scattering by hexagonal ice crystals. *J. Atmos. Sci.*, 38, 1260-1271.

Curran, R. J. and M.-L. C. Wu, 1982: Skylab near-infrared observations of clouds indicating supercooled liquid water droplets. *Jour. Atm. Sci.*, 39, 635-647.

Davies, R., 1984: Reflected solar radiances from broken cloud scenes and the interpretation of scanner measurements. *J. Geophys. Res.*, 89, 1259-1266.

Downing, H. D., and D. Williams, 1975: Optical constants of water in the infrared. *J. Geophys. Res.*, 80, 1656-1661.

Foot, J. S., 1988: Some observations of the optical properties of clouds. II: Cirrus. *Q. J. R. Meteor. Soc.*, 114, 145-164.

Hansen, J. E., and J. B. Pollack, 1970: Infrared light scattering by terrestrial clouds. *J. Atmos. Sci.*, 27, 265-281.

Heymsfield, A. J., 1977: Precipitation development in stratiform ice clouds: A microphysical and dynamical study. *J. Atmos. Sci.*, 34, 367-381.

Heymsfield, A. J., and D. Baumgardner, 1985: Summary of a workshop on processing 2-D probe data. *Bull. Amer. Meteor. Soc.*, 66, 437-440.

Heymsfield, A. J., and L. Miloshevich, 1989: An evaluation of liquid water measuring devices in cold clouds sampled during FIRE. *J. Atmos. Ocean. Tech.*, in press.

Heymsfield, A. J., and C. M. R. Platt, 1984: A parameterization of the particle size spectrum of ice clouds in terms of ambient temperature and the ice water content. *J. Atmos. Sci.*, 41, 846-855.

Heymsfield, A. J., K. M. Miller, and J. D. Spinhirne, 1989: The October 27-28, 1986, FIRE case study: cloud microstructure. Submitted to *Mon. Wea. Rev.*

Iqbal, M., 1983: An Introduction to Solar Radiation. Academic Press, 390pp.

King, M. D., 1987: Determination of the scaled optical thickness of clouds from reflected solar radiation measurements. *J. Atmos. Sci.*, 44, 1734-1751.

Markham, B. L., and J. L. Barker, 1985: Spectral characterization of the LANDSAT Thematic Mapper sensors. *Int. J. Rem. Sens.*, 6, 697-716.

Markham, B. L., and J. L. Barker, 1986: Landsat MSS and TM post-calibration dynamic ranges, exoatmospheric reflectances, and at-satellite temperatures. *EOSAT Landsat Technical Notes*, No. 1, August, 1986.

Palmer, K. F., and D. Williams, 1974: Optical properties of water in the near infrared. *J. Opt. Soc. Amer.*, 64, 1107-1110.

Platt, C. M. R., and G. L. Stephens, 1980: The interpretation of remotely sensed high cloud emittances. *J. Atmos. Sci.*, 37, 2314-2322.

Platt, C. M. R., D. W. Reynolds, and N. L. Abshire, 1980: Satellite and lidar observations of the albedo, emittance, and optical depth of cirrus compared to model calculations. *Mon. Wea. Rev.*, 108, 195-204.

Platt, C. M. R., J. C. Scott, and A. C. Dilley, 1987: Remote sensing of high clouds. Part VI: Optical properties of midlatitude and tropical cirrus. *J. Atmos. Sci.*, 44, 729-747.

Pollack, J. B., and J. N. Cuzzi, 1980: Scattering by nonspherical particles of size comparable to a wavelength: A new semi-empirical theory and its application to tropospheric aerosols. *J. Atmos. Sci.*, 37, 868-881.

Pollack, J. B., D. W. Strecker, F. C. Witterhorn, E. F. Erikson, and B. J. Baldwin, 1978: Properties of the clouds of Venus as inferred from airborne observations of its near-infrared reflectivity spectrum. *Icarus*, 36, 28.

Potter, J. F., 1970: The delta function approximation in radiative transfer theory. *J. Atmos. Sci.*, 27, 943-949.

Reynolds, D. W. and T. H. Vonder Haar, 1977: A bi-spectral method for cloud parameter determination. *Mon. Wea. Rev.*, 105, 446-457.

Rossow, W. B., F. Mosher, E. Kinsella, A. Arking, M. Desbois, E. Harrison, P. Minnis, E. Ruprecht, G. Seze, C. Simmer, and E. Smith, 1985: ISCCP cloud algorithm intercomparison. *J. Clim. Appl. Met.*, 24, 877-903.

Rozenberg, G. V., M. S. Malkevich, M. S. Malkova, and W. I. Syachov, 1974: Determination of the optical characteristics of clouds from measurements of reflected solar radiation on the Kosmos 320 satellite. *Izv. Atm. and Oceanic Phys.*, 10, 14-24.

Sassen, K. and K.-N. Liou, 1979: Scattering of polarized laser light by water droplet, mixed-phase, and ice crystal clouds. Part I: Angular scattering patterns. *J. Atmos. Sci.*, 36, 838-851.

Slater, P. N., S. F. Biggar, R. G. Holm, R. D. Jackson, Y. Mao, M.S. Moran, J. M. Palmer, and B. Yuan, 1987: Reflectance- and radiance-based methods for the in-flight absolute calibration of multispectral sensors. *Rem. Sens. Env.*, 22, 11-37.

Spinhirne, J. D., and W. D. Hart, 1989: ER-2 lidar and spectral radiometer cirrus observations for October 28, 1986. Submitted to *Mon. Wea. Rev.*

Starr, D. O'C., and D. P. Wylie, 1989: The 27-28 October 1986 FIRE case study: Meteorology and cloud fields. Submitted to *Mon. Wea. Rev.*

Suttles, J. T., 1981: Anisotropy of solar radiation leaving the earth-atmosphere system. Ph.D. Thesis, Old Dominion University, Norfolk, VA., 180 pp. Avail. NTIS, NASA Accession No. N82-32242).

Suttles, J. T., 1985: In Radiative Transfer in Scattering and Absorbing Atmospheres. Edited by J. Lenoble, A. Deepak Publishing.

Suttles, J. T., R. N. Green, P. Minnis, G. L. Smith, W. F. Staylor, B. A. Wielicki, I. J. Walker, D. F. Young, V. R. Taylor, and L. L. Stowe, 1988: Angular radiation models for Earth-Atmosphere system. Volume I - shortwave radiation. *NASA Reference Publication* 1184, July, 1988.

Takano, Y., and K-N Liou, 1989: Radiative transfer in cirrus clouds I. single-scattering and optical properties of oriented hexagonal ice crystals. *J. Atmos. Sci*, in press.

Twomey, S., 1971: Radiative transfer: Terrestrial clouds. *J. Quant. Spectros. Radiat. Transfer*, 11, 779-783.

Twomey, S. and T. Cocks, 1982: Spectral reflectance of clouds in the near-infrared: Comparison of measurements and calculations. *J. Met. Soc. Japan*, 60, 583-592.

van de Hulst, H. C., 1957: Light Scattering by Small Particles. Wiley, New York.

Volkovitskiy, O. A., L. N. Pavlova, and A. G. Petrushin, 1980: Scattering of light by ice crystals. *Izvestiya, Atm. and Ocean. Phys.*, 16, 98-102.

Warren, S. G., 1984: Optical constants of ice from the ultraviolet to the microwave. *Appl. Opt.*, 23, 1206-1225.

Wielicki, B. A., 1980: An analysis of cloud property retrieval using infrared sounder data. Ph.D. Thesis, University of California, Nat. Center for Atmos. Research Cooperative Thesis. NCAR/CT-61, 121pp.

Wu, M-L. C., 1985: Quality of remote sensing measurements of cloud physical parameters in the Cooperative Convective Precipitation Experiment. *J. Geophys. Res.*, 90, 10,551-10,562.

FIGURE CAPTIONS

Fig. 1. Location of the Landsat image area for the study. Solid line box gives the 58.4 km square area over Lake Michigan analyzed and shown in Fig. 2.

Fig. 2. Landsat 11.5μm brightness temperatures over the analysis area. Aircraft tracks and observation times are also given in the figure.

Fig. 3. Viewing geometry for Landsat and ER-2 aircraft radiometric observations of the cirrus cloud. Solar zenith angle is 63°.

Fig. 4. Photographs of cirrus particles collected by the King Air on oil coated slides. 4a shows ice crystals collected at 15:51:57 UTC and corresponds to location "2" in Figs. 2, 8, and 15. 4b shows water droplets collected at 15:38:30 UTC, and corresponds to location "1" in Figs. 2, 8, and 15.

Fig. 5. King Air data obtained from 15:38:00 to 16:07:00. a: Ice water content. b: Liquid water content, upper panel Rosemount icing detector, lower panel forward scattering spectrometer probe. c: Mass-weighted median diameter. d: Mean droplet diameter.

Fig. 6. Sabreliner data obtained during racetrack flight patterns from 15:36:30 to 16:25:35 UTC. a: Altitude versus IWC. b: Altitude versus mass-weighted median diameter.

Fig. 7. Comparison of nadir cloud reflectance and beam emittance as measured by Landsat (open circles) with theoretical calculations using Henyey-Greenstein phase functions with g = 0.5, 0.7, 0.86.

Fig. 8. Landsat 0.83μm nadir reflectance over the analysis area. Aircraft tracks and observation times are also given in the figure. Data in Fig. 7 is taken along the ER-2 ground track (center line).

Fig. 9. As in Fig. 7 but for theoretical calculations using a water droplet Mie scattering phase function (r_e=3.8μm) with two values of $\alpha = \beta_{ext}(0.83\mu m)/\beta_{abs}(11.5\mu m)$, and an empirical ice particle scattering phase function (VPP). Solid circles show observations which contain liquid water droplets.

Fig. 10. Single scatter phase functions: Henyey-Greenstein phase functions are shown for asymmetry parameter g = 0.5, 0.7, and 0.86; water

droplet Mie scattering phase function for r_e = 3.8μm; ice particle laboratory phase function, VPP.

Fig. 11. Error bounds for the data in Figs. 7 and 9. Dashed lines show sensitivity of emittance to change in the assumed cloud height of 8.5 km. Curve for $\epsilon_e - \epsilon_a$ shows potential effect of scattering on 11.5μm emittance.

Fig. 12. Intercalibrated nadir reflectance for ER-2 and Landsat along the ER-2 ground track.

Fig. 13. Anisotropic reflectance ratios. Nadir observations are from Landsat, off-nadir observations are from intercalibrated ER-2 data. Model calculations are given for 3 phase functions as described in the text. 13a is for forward scattered radiation, and 13b is for backward scattered radiation.

Fig. 14. Sensitivity of anisotropic reflectance ratio to the assumed cloud altitude. Nominal value used in Fig. 13 is 8.5 km. Values are shown along the ER-2 ground track for the backscatter case.

Fig. 15. Landsat reflectance ratio, R(2.21μm)/R(0.83μm) over the analysis area. Aircraft tracks and observation times are also given in the figure. Data in Figs. 16 and 18 is taken along the King Air ground track.

Fig. 16. Measured and calculated cloud nadir reflectance. Landsat observations are taken along the King Air ground track seen in Fig. 15. Theoretical calculations use the VPP ice scattering phase function and Mie single scatter albedos as a function of particle radius. 16a and 16b give results for R(0.83μm) vs. R(1.65μm) for liquid water (a) and ice (b) refractive index. 16c and 16d give results for R(0.83μm) vs. R(2.21μm) for liquid water (c) and ice (d) refractive index.

Fig. 17. King Air measured cirrus size distributions using the FSSP, 2D-C and 2D-P probes. Particle size for 2D probes is that of a sphere with equivalent cross-section area to the particle 2-D image. Size distributions are averaged over the time intervals shown in the figure.

Fig. 18. Comparison of Landsat measured cloud reflectance ratio R(2.21μm)/R(0.83μm) with the King Air determined effective radius r_e.

Landsat 5: October 28, 1986
15:53 UTC

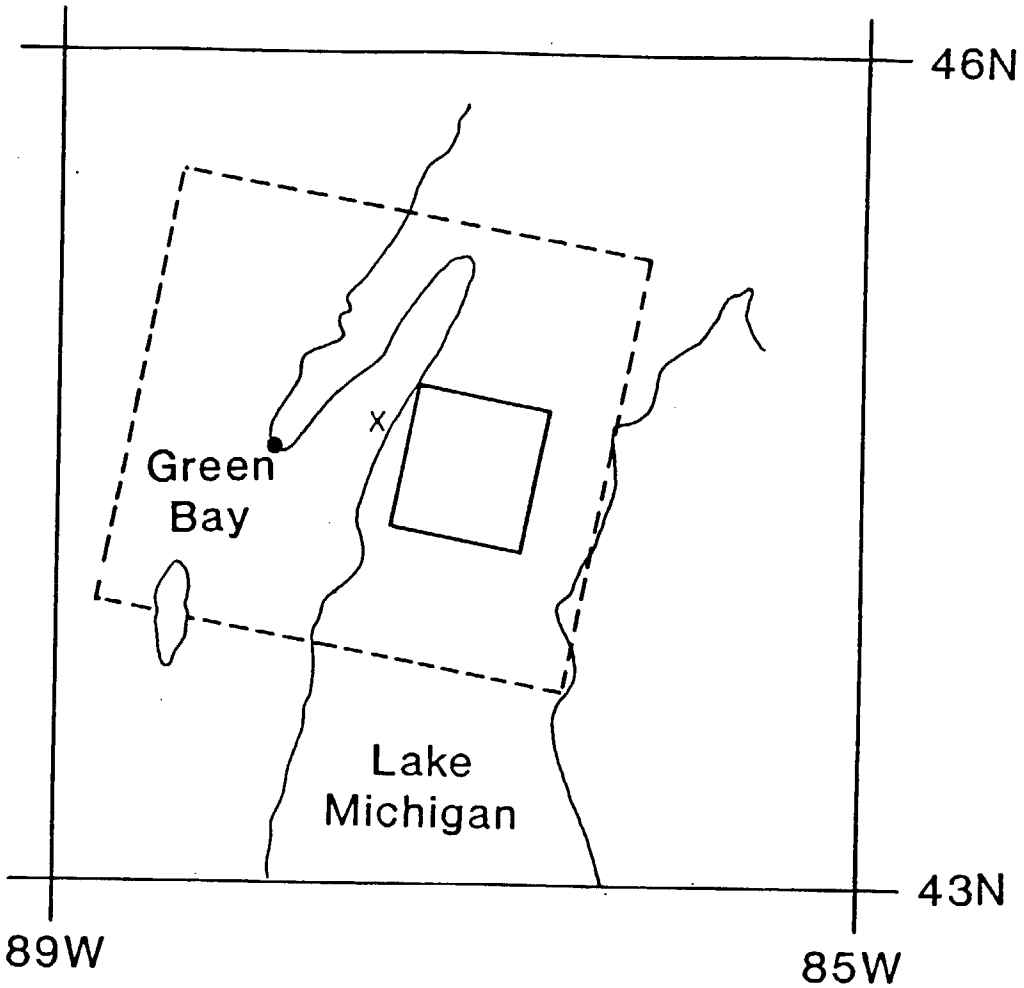

Figure 1

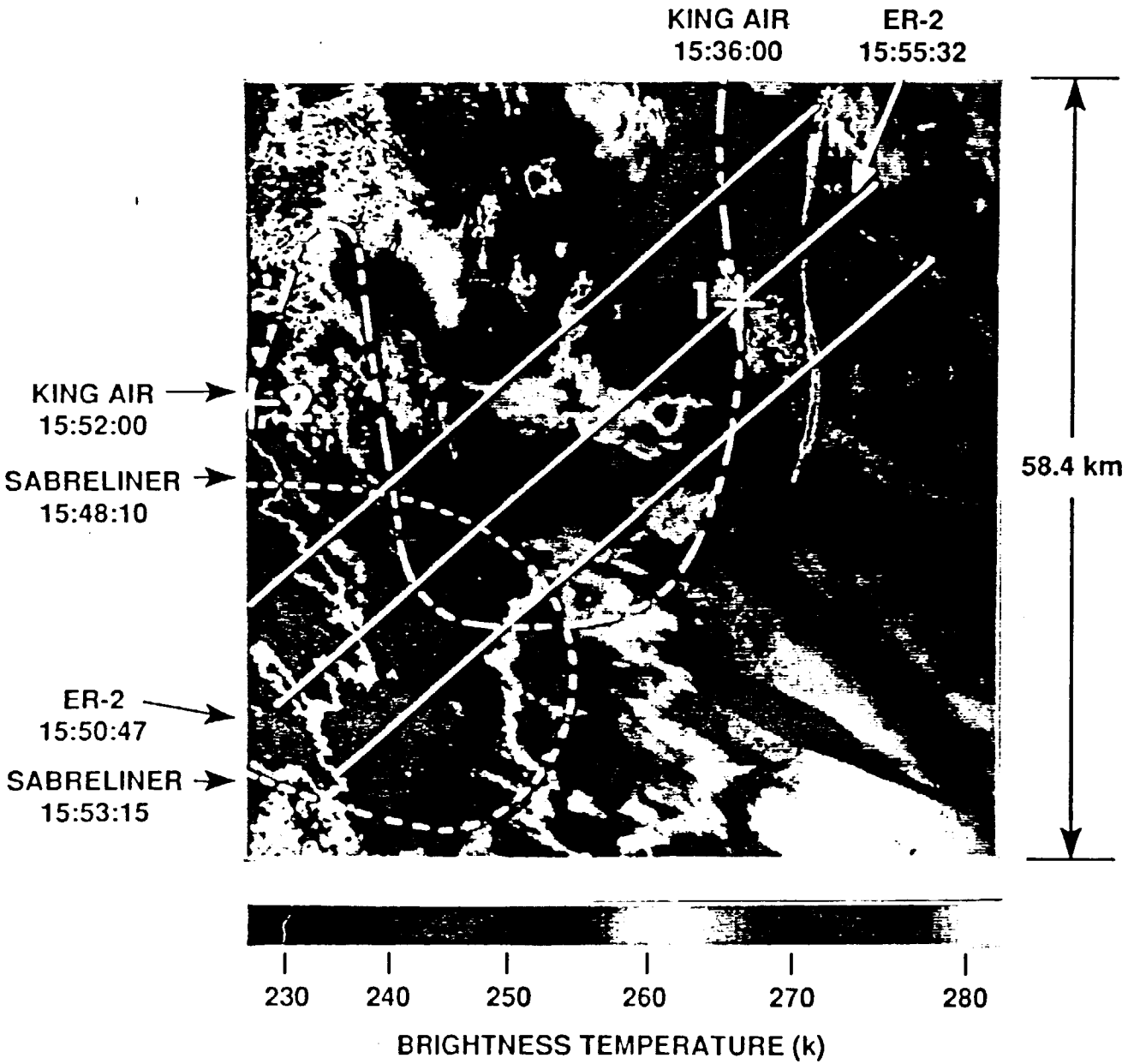
LANDSAT, 11.5 μm, 15:53:12 GMT
KING AIR
15:36:00
ER-2
15:55:32
KING AIR
15:52:00
SABRELINER
15:48:10
ER-2
15:50:47
SABRELINER
15:53:15
58.4 km
230
240
250
260
270
280
BRIGHTNESS TEMPERATURE (k)

Figure 2

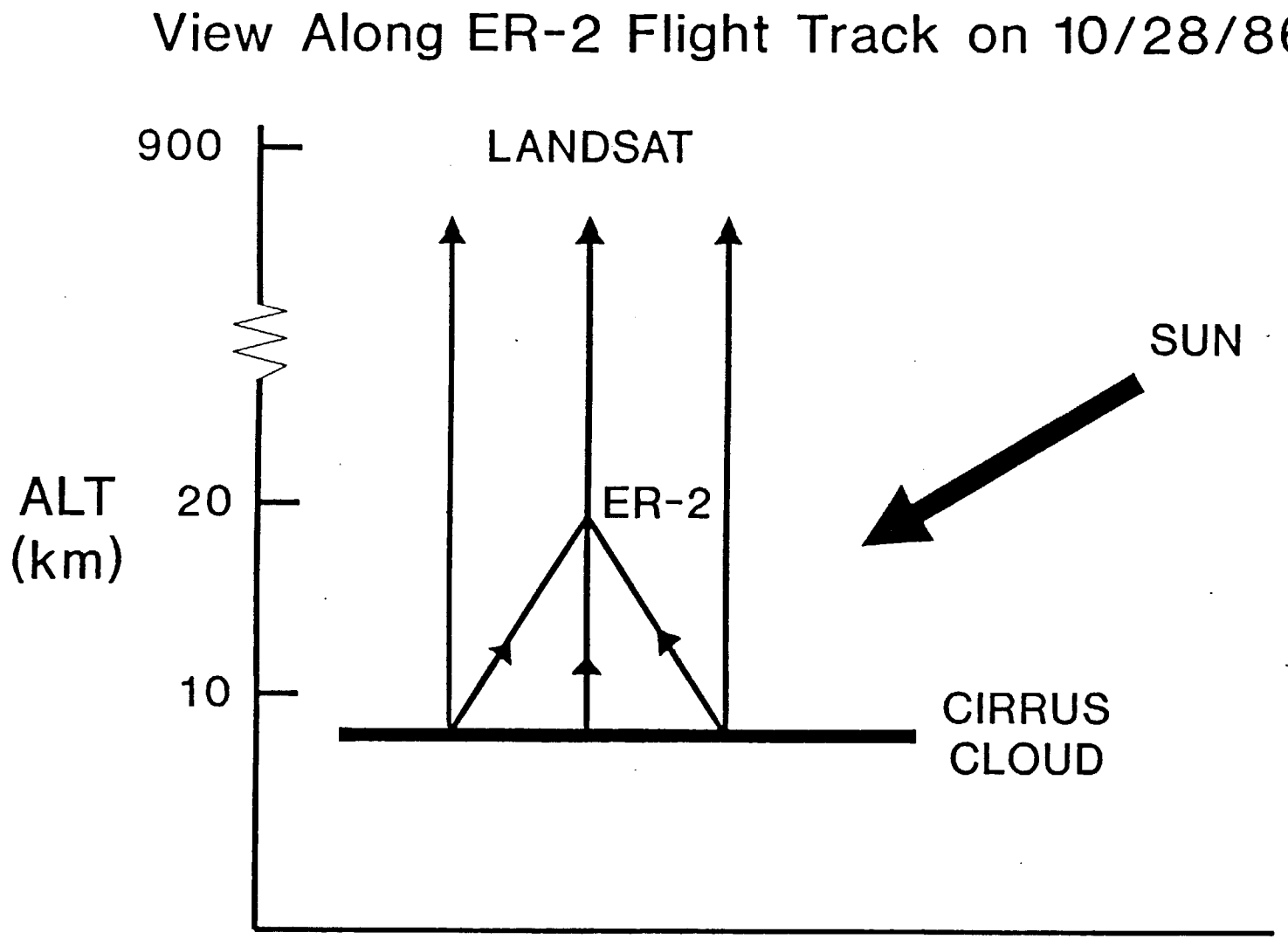
View Along ER-2 Flight Track on 10/28/86
900
LANDSAT
SUN
ALT
(km)
20
ER-2
10
CIRRUS
CLOUD

Figure 3

King Air, 15:51:57 UTC, 7.0 km
-27.8 C

a

King Air, 15:38:30 UTC, 7.3 km
-29.8 C

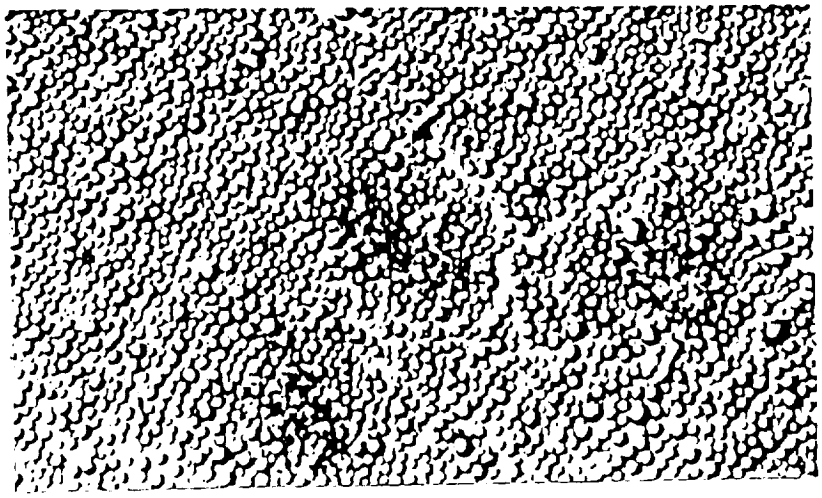

b

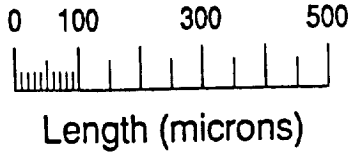

Figure 4

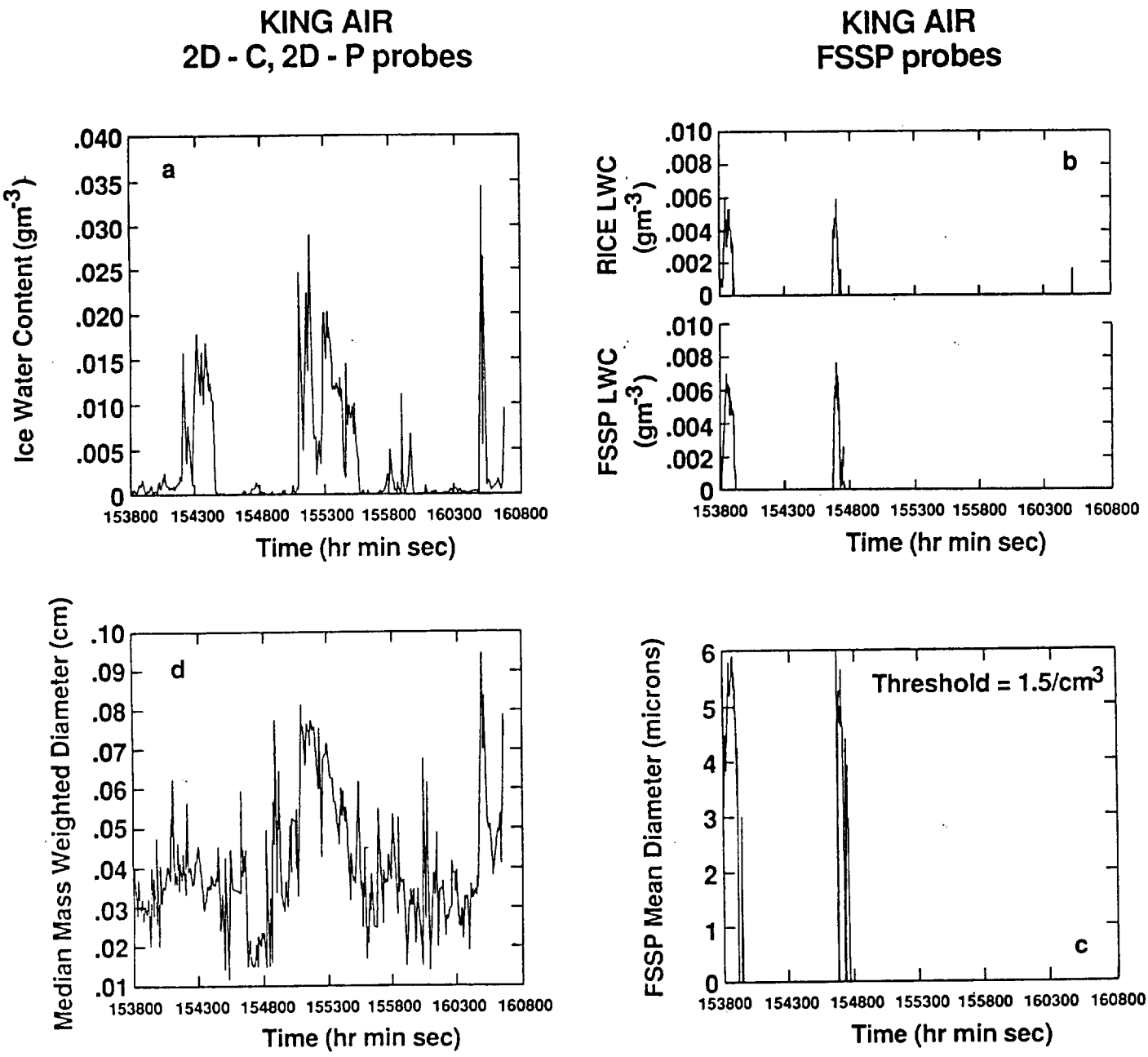
KING AIR
2D - C, 2D - P probes
KING AIR
FSSP probes
Ice Water Content (gm-3)
.040
.035
.030
.025
.020
.015
.010
.005
0
a
153800 154300 154800 155300 155800 160300 160800
Time (hr min sec)
RICE LWC (gm-3)
.010
.008
.006
.004
.002
0
b
FSSP LWC (gm-3)
.010
.008
.006
.004
.002
0
153800 154300 154800 155300 155800 160300 160800
Time (hr min sec)
Median Mass Weighted Diameter (cm)
.10
.09
.08
.07
.06
.05
.04
.03
.02
.01
d
153800 154300 154800 155300 155800 160300 160800
Time (hr min sec)
FSSP Mean Diameter (microns)
6
5
4
3
2
1
0
Threshold = 1.5/cm3
c
153800 154300 154800 155300 155800 160300 160800
Time (hr min sec)

Figure 5

SABRELINER 2D PROBES

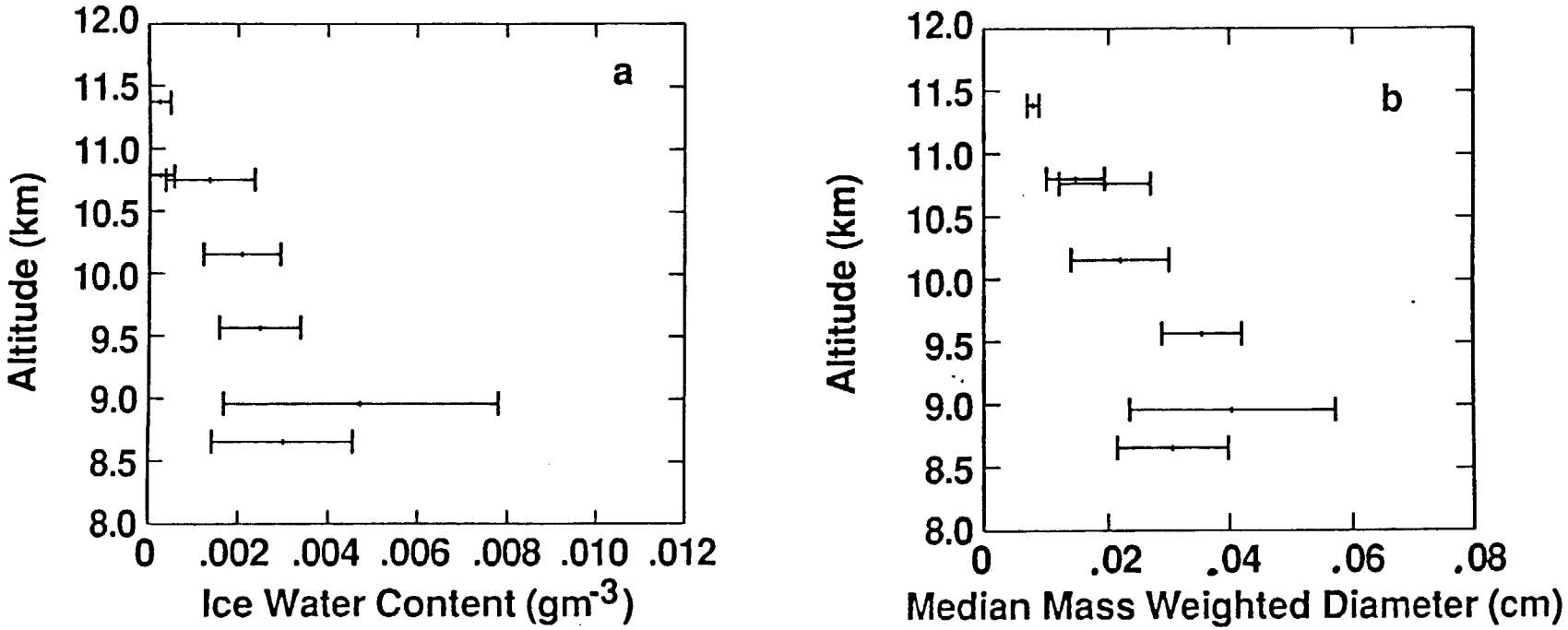

Figure 6

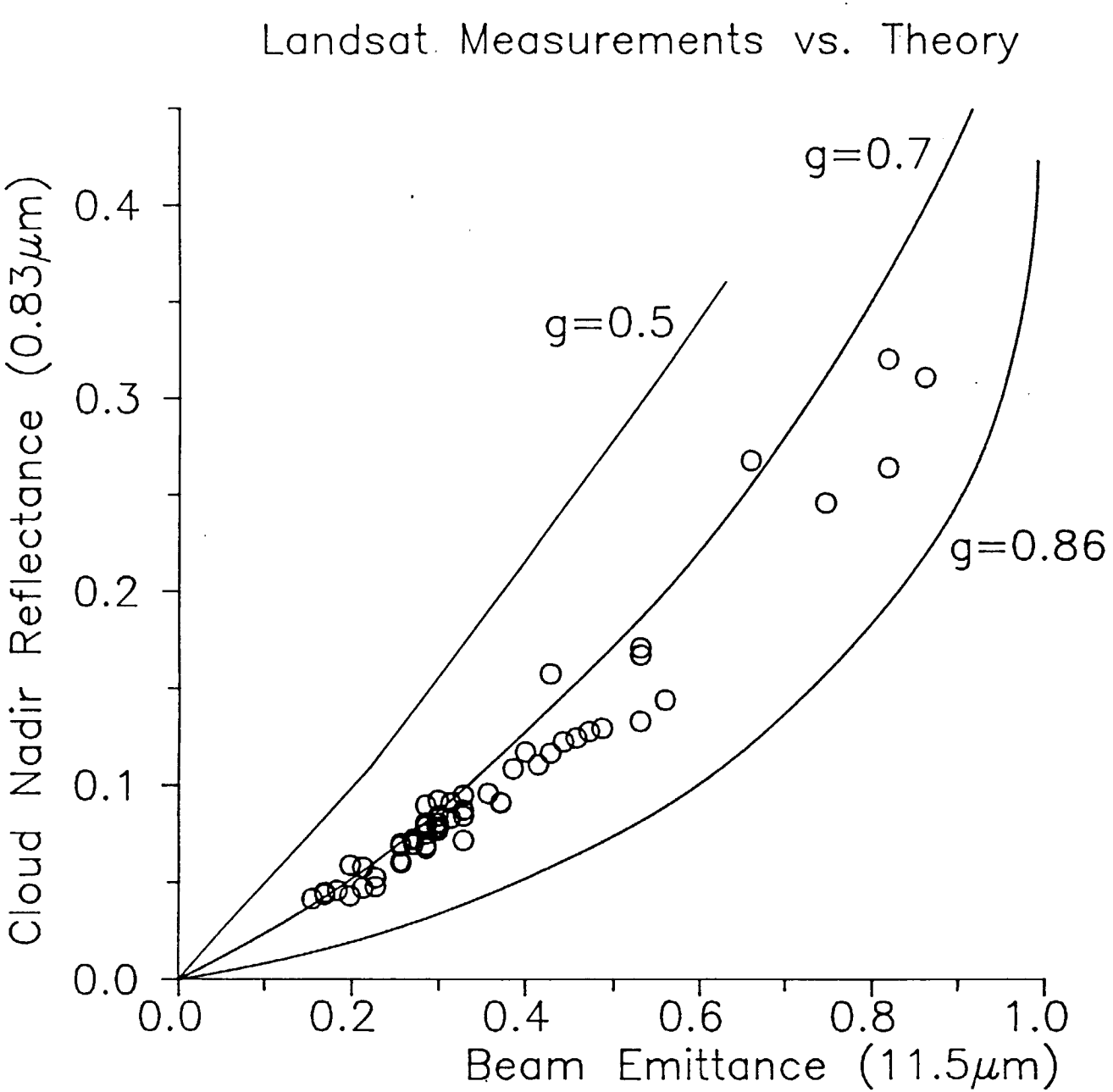
Landsat Measurements vs. Theory
g=0.7
g=0.5
g=0.86
Cloud Nadir Reflectance (0.83μm)
0.0
0.1
0.2
0.3
0.4
0.0
0.2
0.4
0.6
0.8
1.0
Beam Emittance (11.5μm)

Figure 7

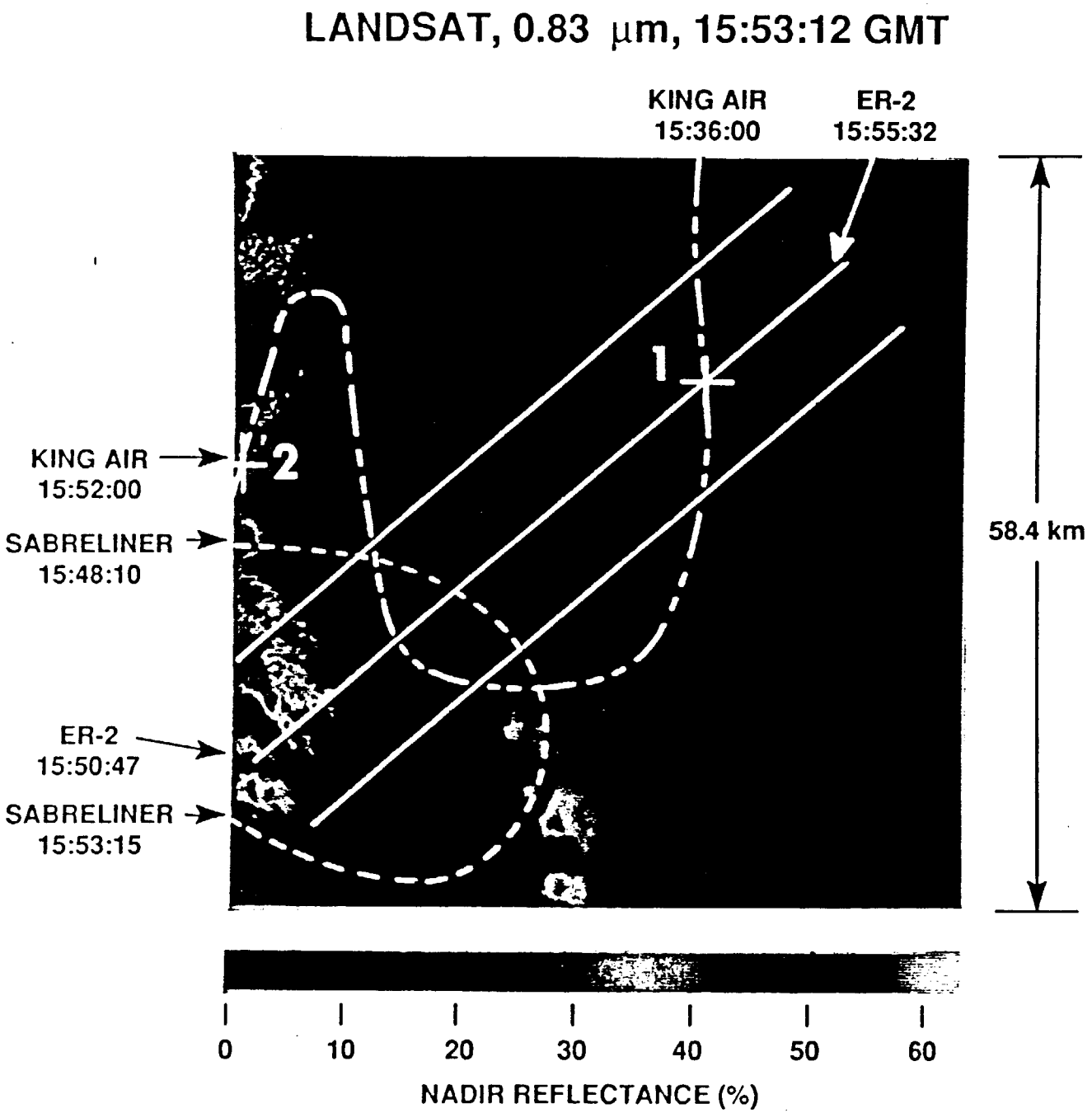
LANDSAT, 0.83 μm, 15:53:12 GMT
KING AIR
15:36:00
ER-2
15:55:32
1
2
KING AIR
15:52:00
SABRELINER
15:48:10
ER-2
15:50:47
SABRELINER
15:53:15
58.4 km
0
10
20
30
40
50
60
NADIR REFLECTANCE (%)

Figure 8

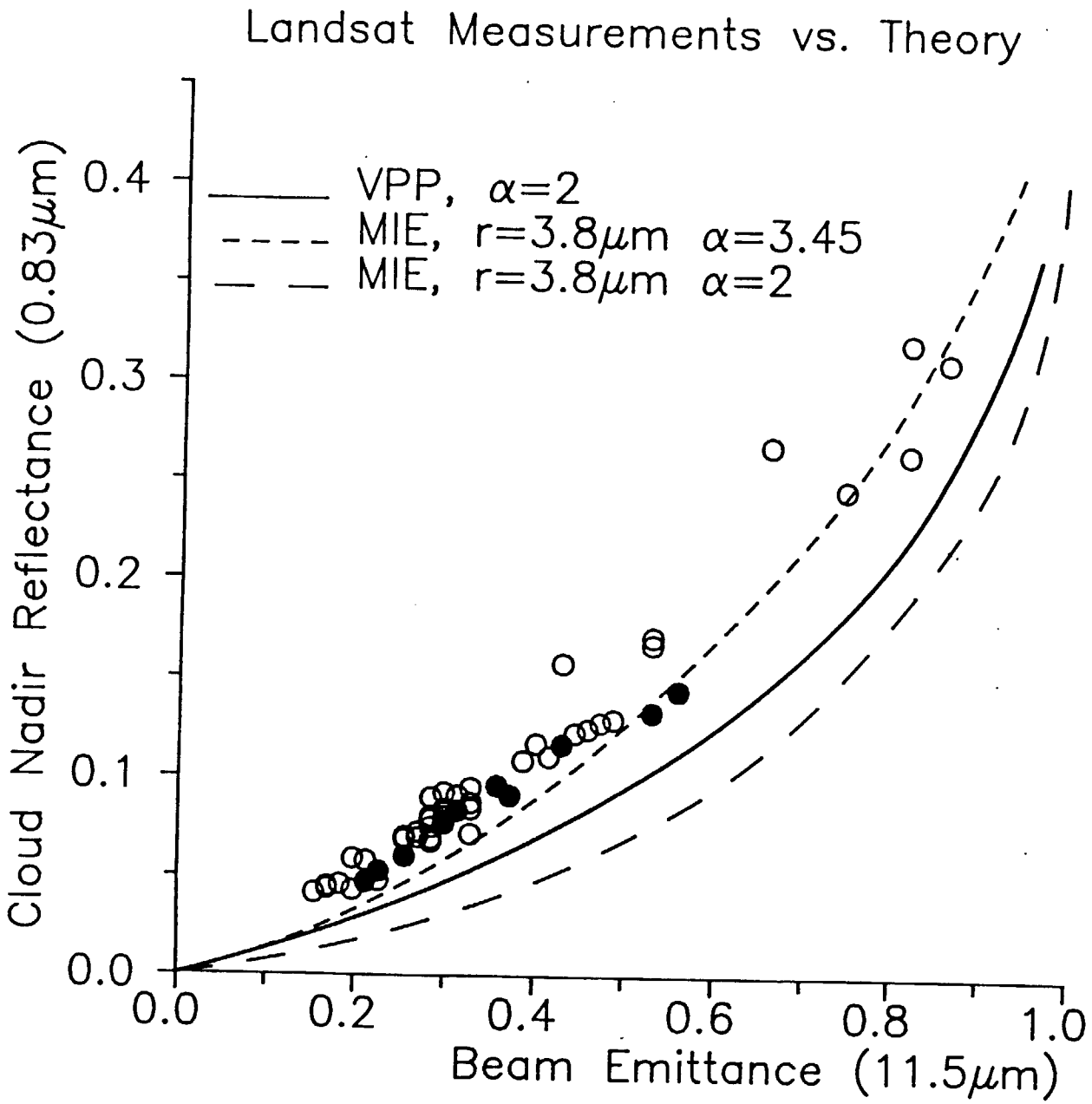
Landsat Measurements vs. Theory
VPP, α=2
MIE, r=3.8μm α=3.45
MIE, r=3.8μm α=2
Cloud Nadir Reflectance (0.83μm)
0.0
0.1
0.2
0.3
0.4
0.0
0.2
0.4
0.6
0.8
1.0
Beam Emittance (11.5μm)

Figure 9

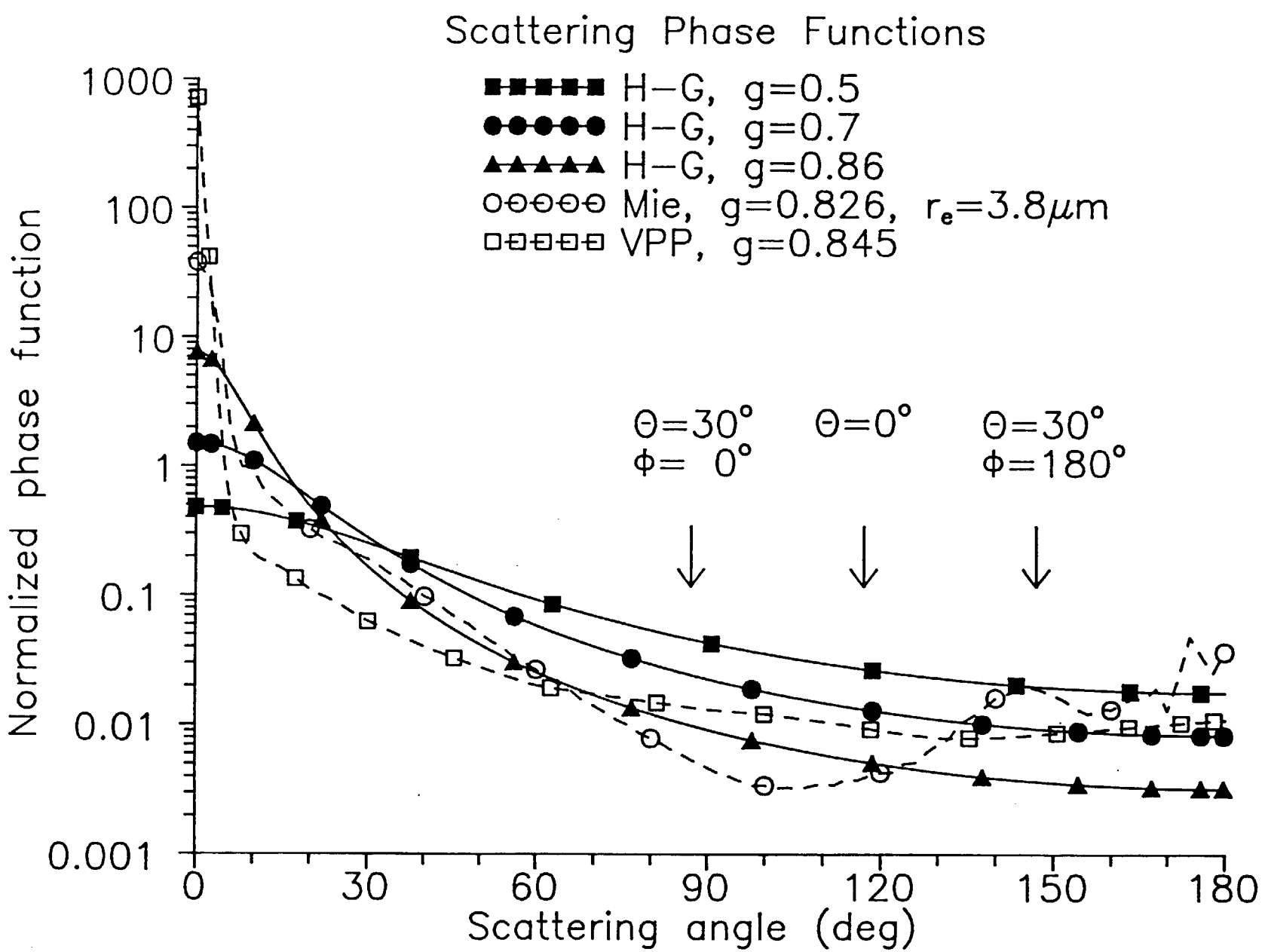
Scattering Phase Functions
H–G, g=0.5
H–G, g=0.7
H–G, g=0.86
Mie, g=0.826, r_e=3.8μm
VPP, g=0.845
Θ=30° Φ= 0°
Θ=0°
Θ=30° Φ=180°
Normalized phase function
1000
100
10
1
0.1
0.01
0.001
0
30
60
90
120
150
180
Scattering angle (deg)

Figure 10

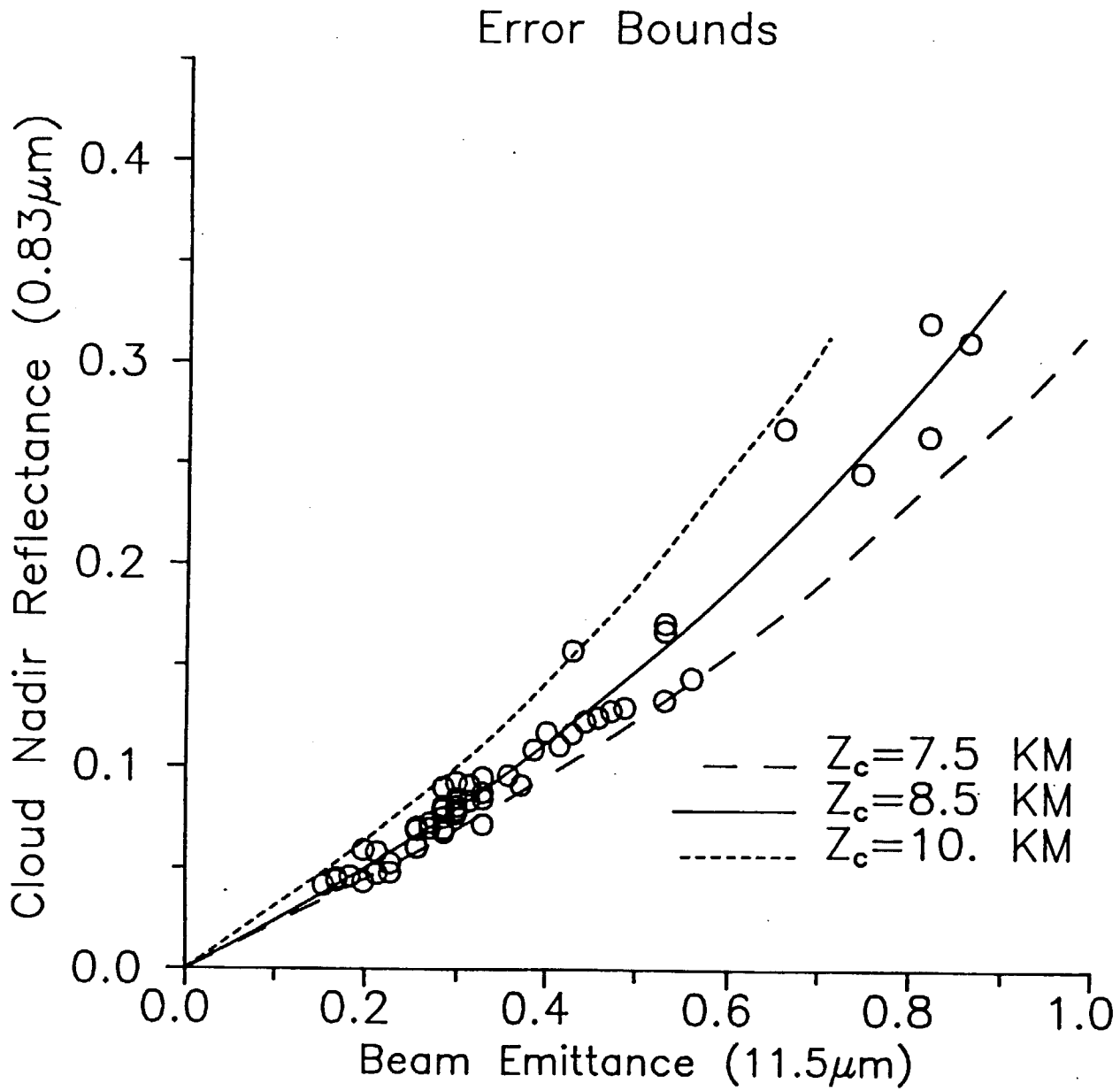
Error Bounds
Cloud Nadir Reflectance (0.83μm)
0.0
0.1
0.2
0.3
0.4
0.0
0.2
0.4
0.6
0.8
1.0
Beam Emittance (11.5μm)
Zc=7.5 KM
Zc=8.5 KM
Zc=10. KM

Figure 11

Figure 12

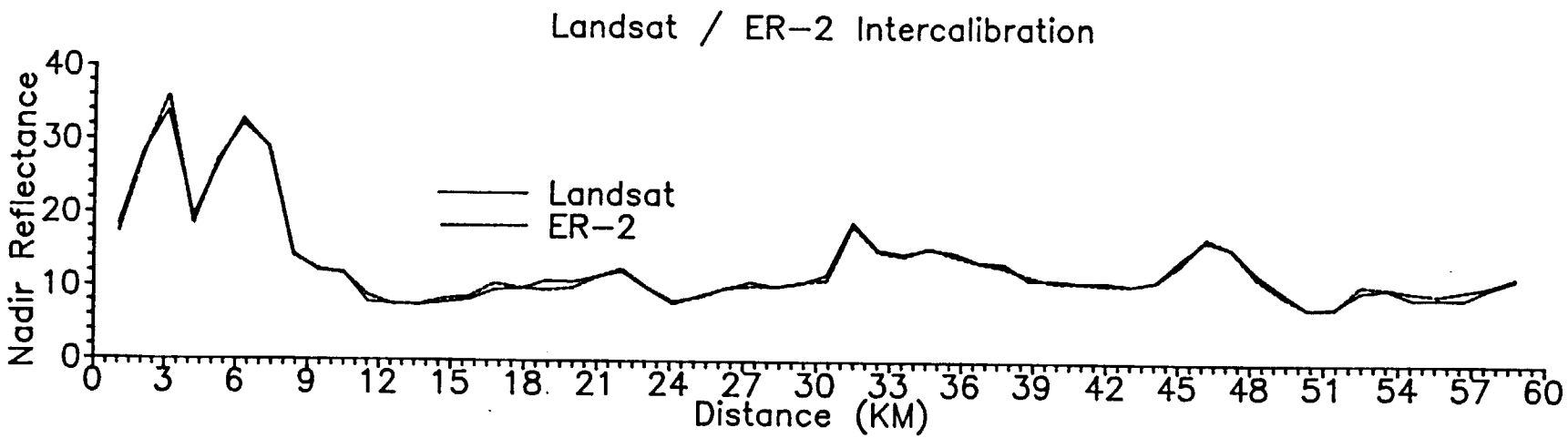
Landsat / ER–2 Intercalibration
Nadir Reflectance
40
30
20
10
0
Landsat
ER–2
0 3 6 9 12 15 18 21 24 27 30 33 36 39 42 45 48 51 54 57 60
Distance (KM)

Reflectance Anisotropy

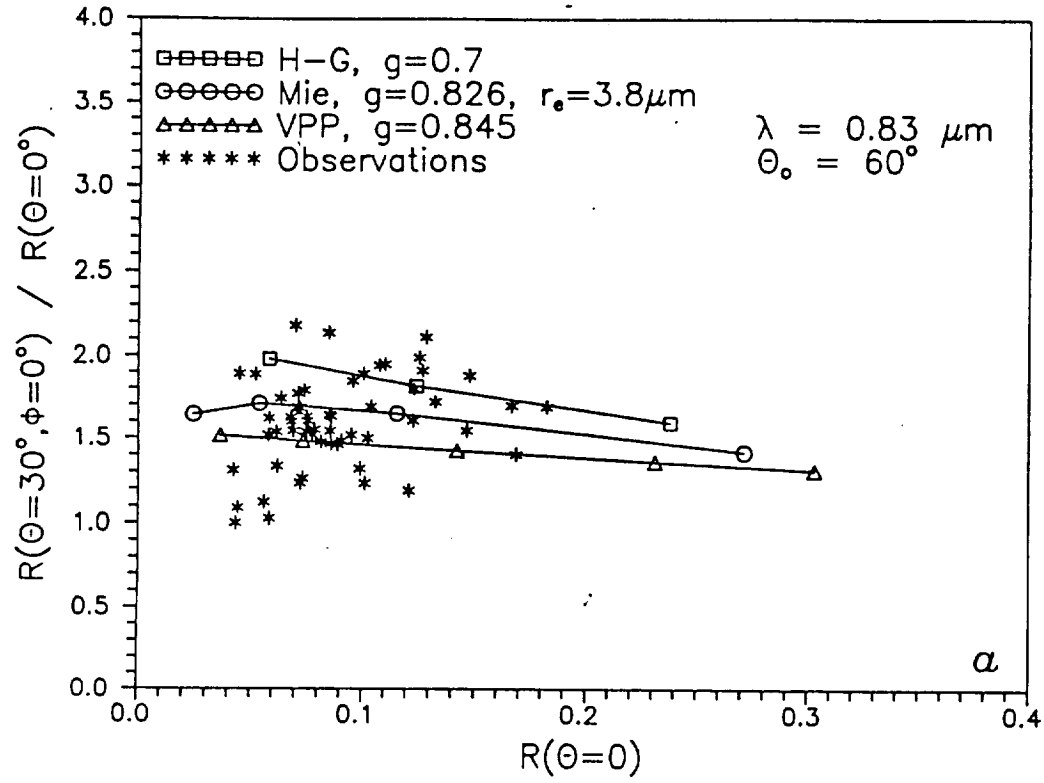

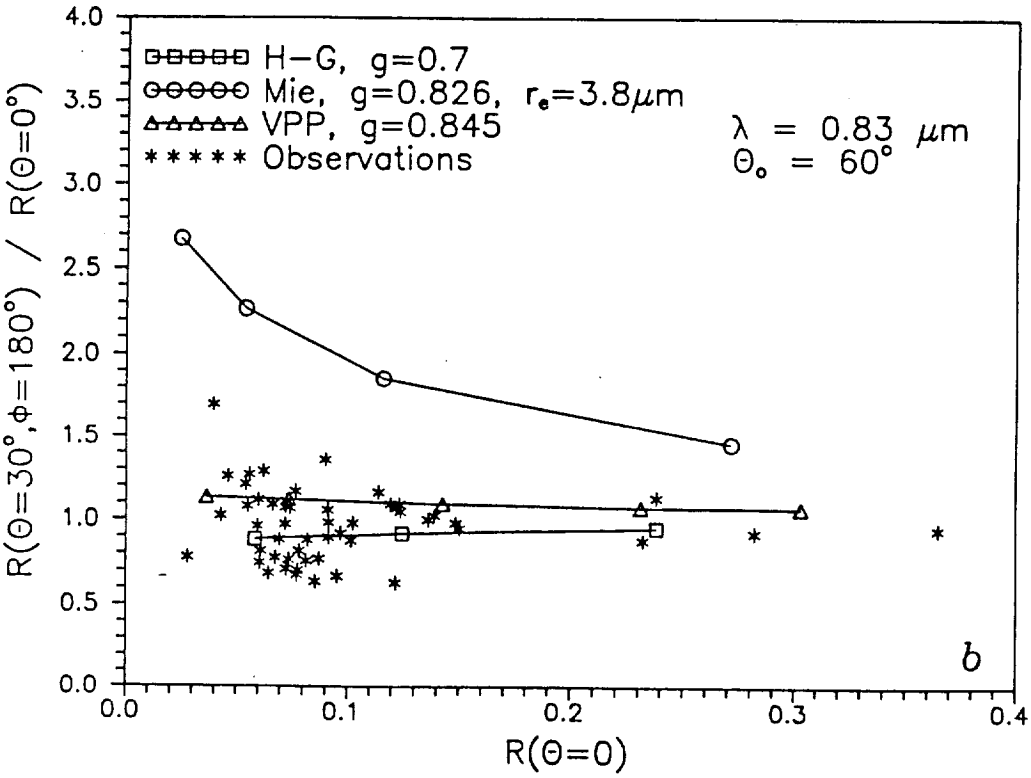

Figure 13

Figure 14

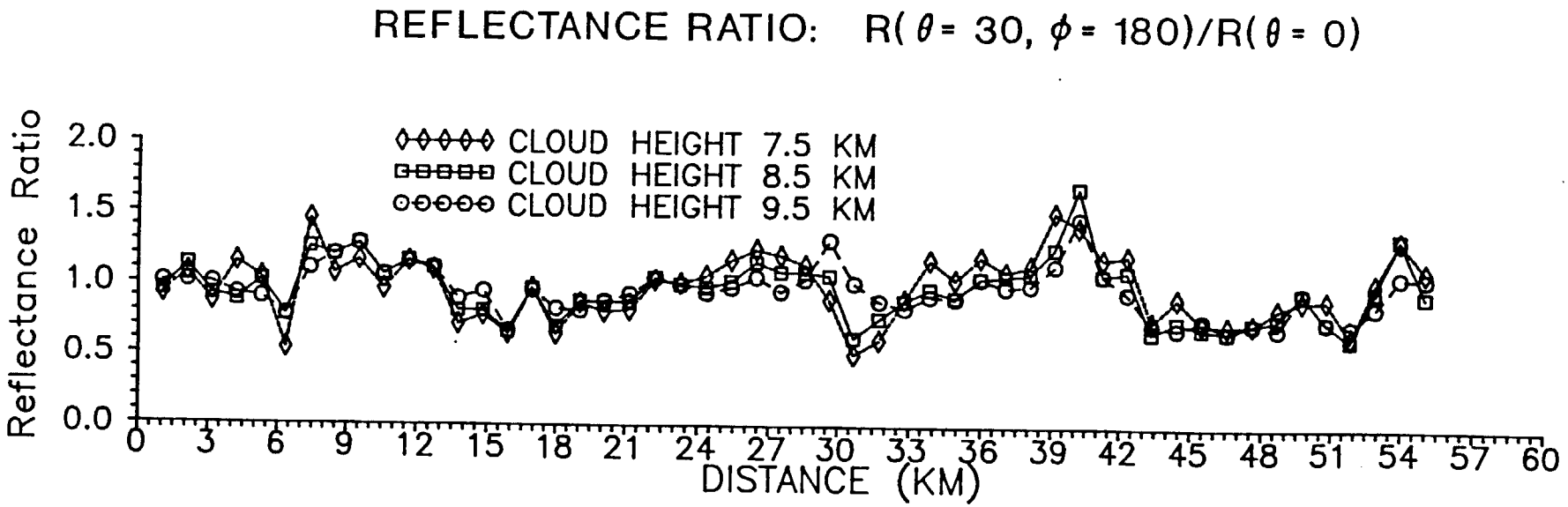
REFLECTANCE RATIO: R(θ = 30, φ = 180)/R(θ = 0)
CLOUD HEIGHT 7.5 KM
CLOUD HEIGHT 8.5 KM
CLOUD HEIGHT 9.5 KM
Reflectance Ratio
2.0
1.5
1.0
0.5
0.0
0 3 6 9 12 15 18 21 24 27 30 33 36 39 42 45 48 51 54 57 60
DISTANCE (KM)

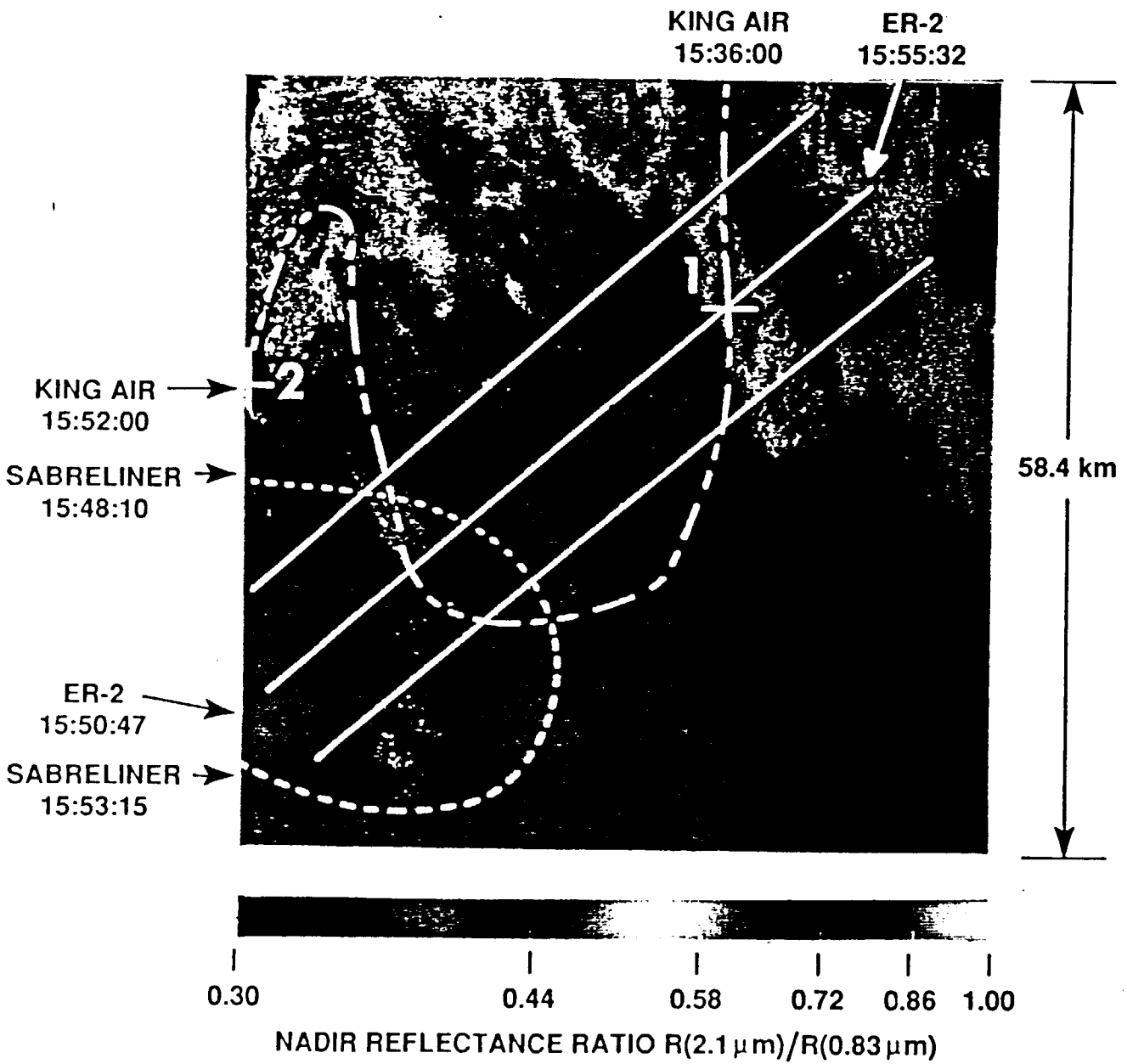
LANDSAT, R(2.1 μm)/R(0.83 μm), 15:53:12 GMT
KING AIR
15:36:00
ER-2
15:55:32
1
2
KING AIR
15:52:00
SABRELINER
15:48:10
ER-2
15:50:47
SABRELINER
15:53:15
58.4 km
0.30
0.44
0.58
0.72
0.86
1.00
NADIR REFLECTANCE RATIO R(2.1 μm)/R(0.83 μm)

Figure 15

Landsat Particle Size Estimation along the King Air track

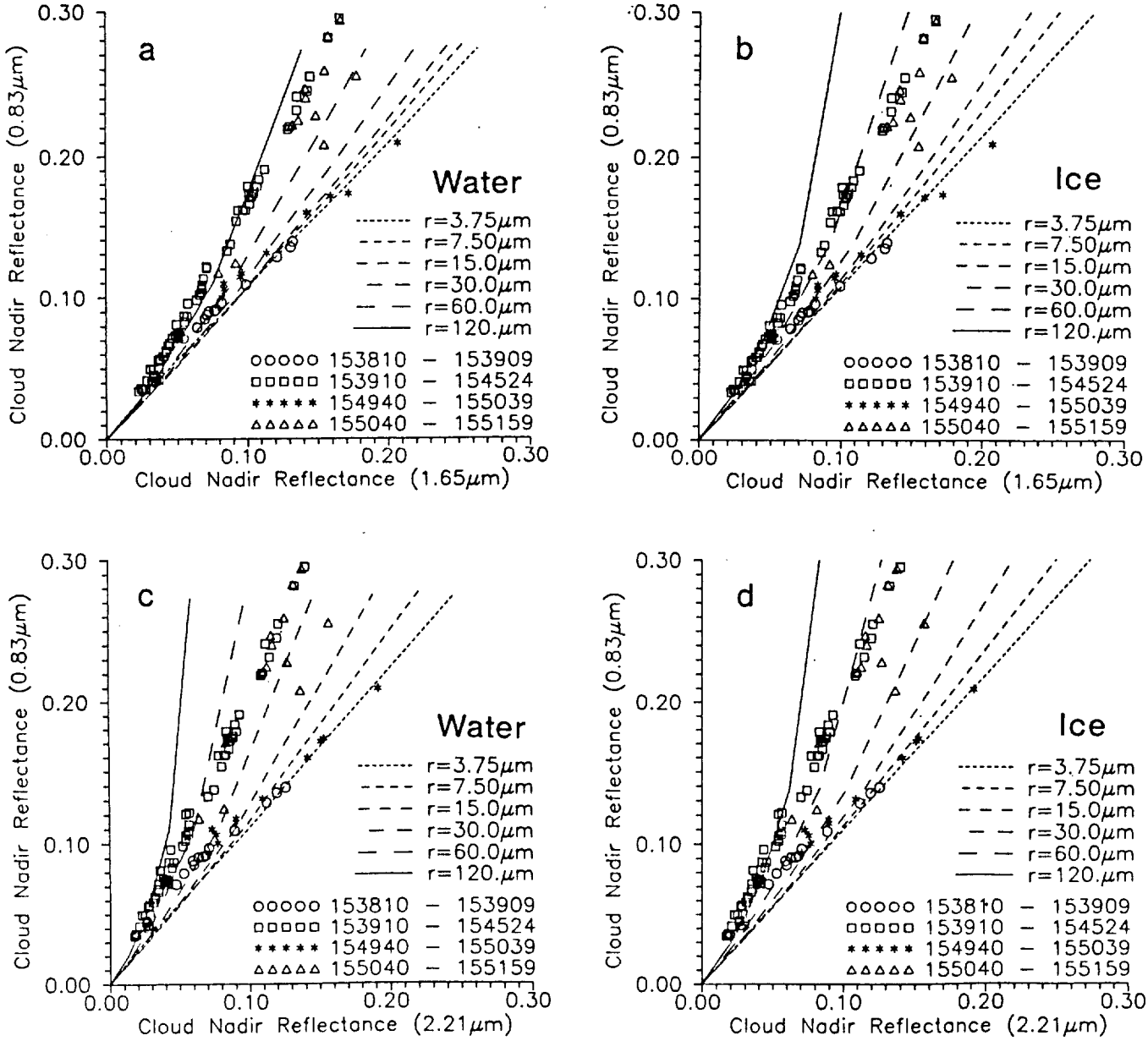

Figure 16

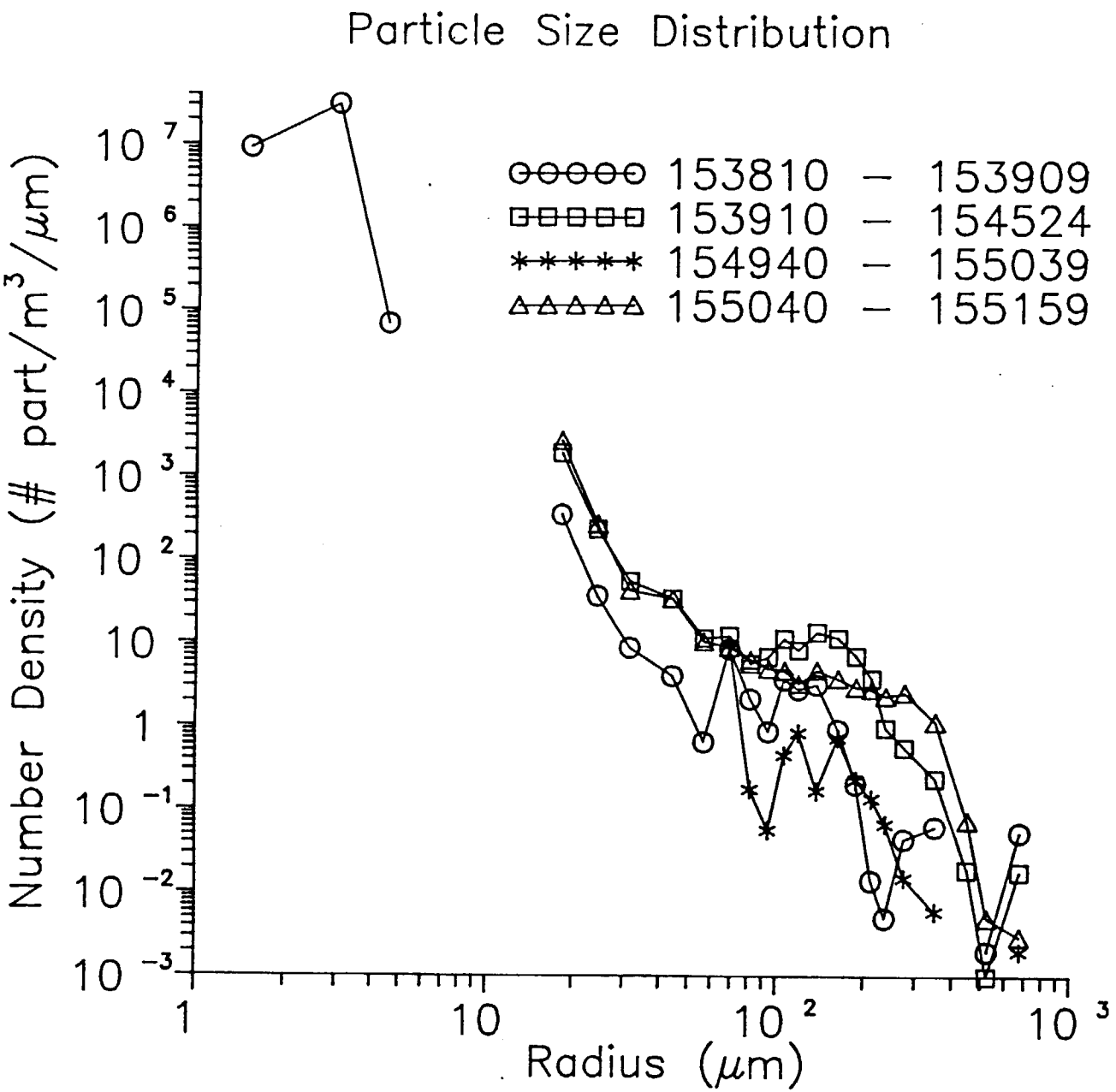
Particle Size Distribution
153810 – 153909
153910 – 154524
154940 – 155039
155040 – 155159
Number Density (# part/m^3/μm)
10^7
10^6
10^5
10^4
10^3
10^2
10
1
10^{-1}
10^{-2}
10^{-3}
1
10
10^2
10^3
Radius (μm)

Figure 17

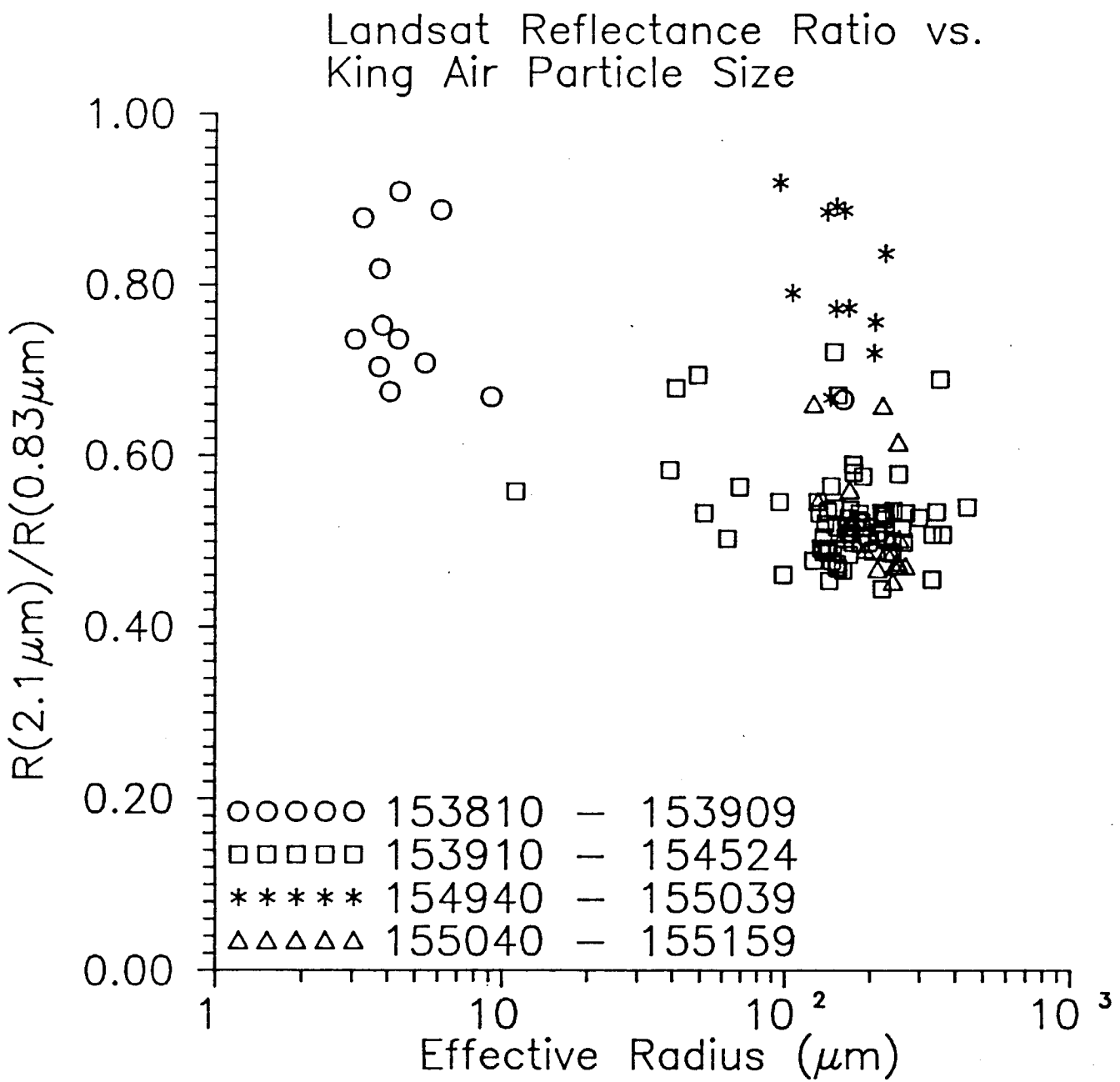
Landsat Reflectance Ratio vs.
King Air Particle Size
1.00
0.80
0.60
0.40
0.20
0.00
R(2.1μm)/R(0.83μm)
ooooo 153810 – 153909
□□□□□ 153910 – 154524
***** 154940 – 155039
ΔΔΔΔΔ 155040 – 155159
1
10
10 2
10 3
Effective Radius (μm)

Figure 18